AD-A113 982 ENVIRONMENTAL RESEARCH INST OF MICHIGAN ANN ARBOR RA--ETC F/G 14/5
DESIGN STUDY FOR A LOW-DISTORTION HOLOGRAPHIC HUD.(U)
JAN 82 W S COLBURN, R C FAIRCHILD F33615-80-C-1077
UNCLASSIFIED ERIM-150800-29-F AFWAL-TR-81-1263 NL

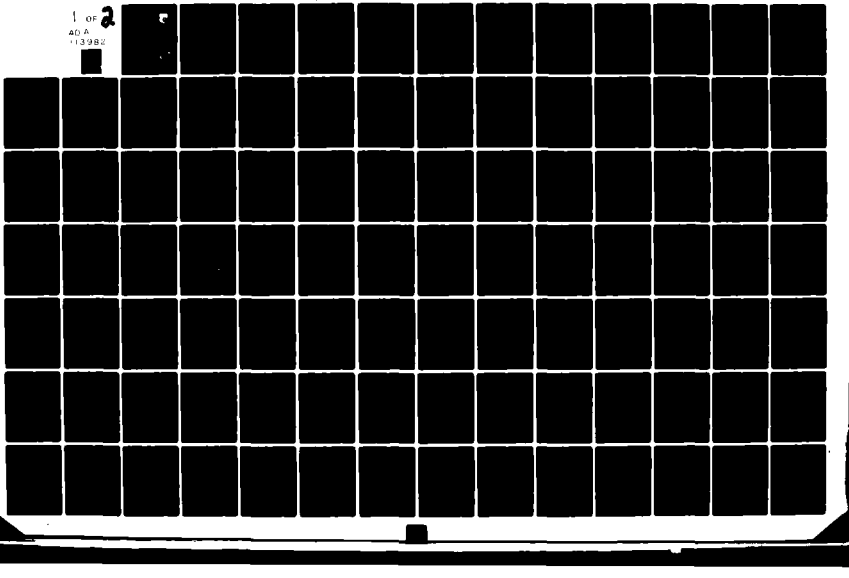

(12)

AFWAL-TR-81-1263

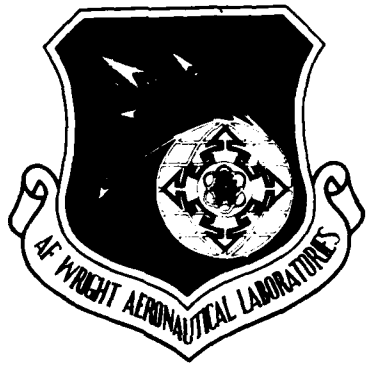


# DESIGN STUDY FOR A LOW-DISTORTION HOLOGRAPHIC HUD

W.S. Colburn, R.C. Fairchild

RADAR AND OPTICS DIVISION
ENVIRONMENTAL RESEARCH INSTITUTE OF MICHIGAN
P.O. Box 8618, Ann Arbor, Michigan 48107

January 1982

Final Technical Report for Period July 1980-August 1981







AVIONICS LABORATORY
AIR FORCE WRIGHT AERONAUTICAL LABORATORIES
AIR FORCE SYSTEMS COMMAND
WRIGHT-PATTERSON AIR FORCE BASE, OHIO 45433

*NOTICE*

*When Government drawings, specifications, or other data are used for any purpose other than in connection with a definitely related Government procurement operation, the United States Government thereby incurs no responsibility nor any obligation whatsoever; and the fact that the government may have formulated, furnished, or in any way supplied the said drawings, specifications, or other data, is not to be regarded by implication or otherwise as in any manner licensing the holder or any other person or corporation, or conveying any rights or permission to manufacture use, or sell any patented invention that may in any way be related thereto.*

*This report has been reviewed by the Office of Public Affairs (ASD/PA) and is releasable to the National Technical Information Service (NTIS). At NTIS, it will be available to the general public, including foreign nations.*

*This technical report has been reviewed and is approved for publication.*

John F. Coonrod

JOHN F. COONROD
Project Engineer, Information Processing Branch
AVIONICS LABORATORY

Donald L. Moon

DONALD L. MOON
Information Processing Technology Branch
AVIONICS LABORATORY

*FOR THE COMMANDER*

Richard H Boivin

RICHARD H. BOIVIN, Col, USAF
Chief, System Avionics Division
Avionics Laboratory

*"If your address has changed, if you wish to be removed from our mailing list, or if the addressee is no longer employed by your organization please notify* AFWAL/AAAT, *W-PAFB, OH 45433 to help us maintain a current mailing list".*

*Copies of this report should not be returned unless return is required by security considerations, contractual obligations, or notice on a specific document.*

AIR FORCE/56780/19 April 1982 — 110

UNCLASSIFIED

SECURITY CLASSIFICATION OF THIS PAGE (When Data Entered)

| REPORT DOCUMENTATION PAGE | | READ INSTRUCTIONS BEFORE COMPLETING FORM |
|---|---|---|
| 1. REPORT NUMBER<br>AFWAL-TR-81-1263 | 2. GOVT ACCESSION NO. | 3. RECIPIENT'S CATALOG NUMBER |
| 4. TITLE (and Subtitle)<br>DESIGN STUDY FOR A LOW-DISTORTION HOLOGRAPHIC HUD | | 5. TYPE OF REPORT & PERIOD COVERED<br>Final Technical Report<br>July 1980 - August 1981 |
| | | 6. PERFORMING ORG. REPORT NUMBER<br>150800-29-F |
| 7. AUTHOR(s)<br>W. S. Colburn, R. C. Fairchild | | 8. CONTRACT OR GRANT NUMBER(s)<br>F33615-80-C-1077 |
| 9. PERFORMING ORGANIZATION NAME AND ADDRESS<br>Environmental Research Institute of Michigan<br>Box 8618, Ann Arbor, MI 48107 | | 10. PROGRAM ELEMENT, PROJECT, TASK AREA & WORK UNIT NUMBERS<br>ILIR 00 09 |
| 11. CONTROLLING OFFICE NAME AND ADDRESS<br>Air Force Wright Aeronautical Laboratories<br>(AFWAL/AAAT) Wright-Patterson AFB, OH 45433 | | 12. REPORT DATE<br>January 1982<br>13. NUMBER OF PAGES<br>96 |
| 14. MONITORING AGENCY NAME & ADDRESS(if different from Controlling Office) | | 15. SECURITY CLASS. (of this report)<br>N/A<br>15a. DECLASSIFICATION/DOWNGRADING SCHEDULE |

16. DISTRIBUTION STATEMENT (of this Report)

Approved for public release; distribution unlimited.

17. DISTRIBUTION STATEMENT (of the abstract entered in Block 20, if different from Report)

18. SUPPLEMENTARY NOTES

19. KEY WORDS (Continue on reverse side if necessary and identify by block number)

Holographic optics
Holographic HUD
Head-up display

20. ABSTRACT (Continue on reverse side if necessary and identify by block number)

- A design investigation was conducted for a low-distortion holographic HUD optical system. Distortion correction was based on the use of a holographic combiner made with analytically defined construction wavefronts, wavefronts for which the phase at the hologram is described by means of a mathematical expression such as a power series expansion. Such wavefronts are designed subsequent to the hologram design, and offer great design flexibility as their realization is based in part on the use of computer generated holograms.

(over)

DD FORM 1 JAN 73 1473 EDITION OF 1 NOV 65 IS OBSOLETE

UNCLASSIFIED

SECURITY CLASSIFICATION OF THIS PAGE (When Data Entered)

20. ABSTRACT (continued)

A method is described for designing the construction wavefronts of a holographic optical element based on minimizing the mean-squared wavefront error while satisfying the Bragg condition. A holographic HUD optical system was designed for the F-16 cockpit in which distortion was corrected optically through simultaneous optimization of combiner and relay lens parameters. Both construction wavefronts of the combiner were described in terms of Legendre polynomial series. A detailed and complete description of the construction wavefronts is included, with ray traces indicating the shapes of the wavefronts. The system design met the distortion goal of 0.5%, or less, over most of the instantaneous field-of-view (12°V x 20°H); design results are presented, including distortion, ray errors, and hologram efficiency. A discussion is included of the implementation of construction beams required to form the combiner construction wavefronts.

"Diffraction Optics Design Study"

## FOREWORD

This report was prepared by the Electro-Optics Department, Radar and Optics Division of the Environmental Research Institute of Michigan. The work was sponsored by the Avionics Laboratory under Contract No. F33615-80-C-1077, Project No. ILI R0009. This program was funded from Laboratory Director's Funds.

The report covers work performed between 15 July 1980 and 30 August 1981. The contract monitor was Mr. John Coonrod, AFWAL/AAAT. The principal investigator was W.S. Colburn. Additional contributors to the technical effort were D.M. Brown, R.C. Fairchild, H.R. Padgitt, and K.A. Winick.

TABLE OF CONTENTS

LIST OF ILLUSTRATIONS

LIST OF ILLUSTRATIONS
(Continued)



LIST OF TABLES

# SECTION I
# INTRODUCTION AND SUMMARY

The holographic Head-Up Display (HUD) offers performance improvements over conventional HUD systems in two respects: the light losses in the combiner are greatly reduced, and the field-of-view is increased. Asymmetries that result from the off-axis nature of the holographic combiner, however, aggravate image abberations and cause a significant amount of geometric distortion in the imagery. Although it is possible to provide distortion correction electronically at the display source, optical correction is preferable to reduce the complexity of the required electronics, in particular where the display source is a matrix type of display device. In previous holographic HUD systems, much of the distortion introduced by the hologram has been corrected by the relay optics. In this report, we present the results of a design investigation of a low-distortion holographic HUD optical system in which distortion was corrected in the holographic combiner as well as in the relay lens. To accomplish this, we assumed the combiner to be a holographic, or diffractive, optical element formed with analytically defined construction wavefronts.

Analytically defined construction wavefronts offer superior flexibility and ease of design compared to previous methods of design using complicated construction beams. In the new method, the phase of each construction wavefront at the hologram surface is established directly by means of a mathematical description, such as a power series expansion; the actual construction beam is not designed until the hologram design is complete. The analytical description of the wavefronts, furthermore, permits the use of wavefronts that are difficult or impossible to realize with conventional optical systems. These wavefronts are implemented through the use of computer generated holograms in the construction beams, with conventional optical

elements providing the major wavefront curvature and the computer generated hologram adding smaller phase perturbations to the wavefront.

This report describes a research program that included an investigation of aspheric holograms made with analytically defined construction beams and the design of a low-distortion holographic HUD. The aspheric hologram investigation developed a general method for designing the construction wavefronts of a holographic optical element based on minimizing the mean-squared phase error in the image formed by the hologram while satisfying the Bragg condition. Consideration was given to the physical realizability of the wavefronts found by the design method. This investigation is described in Section II of the report.

A low-distortion holographic HUD optical system was designed to fit the configuration of the F-16 cockpit. The combiner was designed by describing the phase of each construction wavefront in terms of a series of Legendre polynomials. The optical system included a seven-element relay lens to form an intermediate image of the display, aberrated in such a manner as to compensate for the combiner aberrations. Reduction of both distortion and image errors was carried out through computer optimization of the hologram and relay lens parameters. The design procedures are described in Sections III and IV, which include the complete design parameters of the optical system.

Section V is a discussion of the system performance, including distortion, ray errors, and hologram efficiency. Over most of the instantaneous field-of-view, the distortion met the goal of 0.5 percent or less. Ray errors tended to be somewhat higher than the goals, with accuracy errors generally smaller than parallax errors. The hologram efficiency was satisfactory over most of the field-of-view and at most head locations.

Because the construction wavefronts of the holographic combiner were described as mathematical expressions at the hologram surface only, in Section VI, we discuss realization of such construction beams, including a discussion of the requirements on the computer generated hologram.

In Section VII, we present our conclusions and recommendations. A major conclusion is that distortion correction is feasible in a holographic HUD that uses an aspheric hologram as the combiner. The positive results of this study suggest continued investigation of the aspheric holographic element both at a basic level and as applied in optical systems such as the head-up display.

## SECTION II
## INVESTIGATION OF ASPHERIC HOLOGRAMS

This section summarizes the results of an investigation of design methods for aspheric holograms. In a previous research effort [1], it was shown experimentally that a holographic lens having one of its recording wavefronts defined by a general power series expansion could achieve significantly improved performance over a finite field as compared to a conventional holographic optical element (HOE). A conventional HOE is defined to be a HOE for which both recording wavefronts are spherical, as depicted by Figure 1a. It should be noted that a plane wavefront is considered to be a spherical wavefront with an infinite radius of curvature. An aspheric HOE, on the other hand, is defined to be a HOE for which one or both recording beams are nonspherical, as shown in Figure 1b. We emphasize that the spherical and aspheric descriptors do not refer to the substrate of the hologram, which in either case, may be flat or curved.

In previous holographic HUD investigations [2], aspheric construction wavefronts have been obtained by the introduction of conventional optical elements, often anamorphic, into the construction beams. In this report, the term aspheric HOEs refers to elements made with construction wavefronts that are analytically defined. For these wavefronts, we describe the phase at the hologram surface in terms of a mathematical expression, such as a power series expansion.

Because of the additional degrees of freedom available in the construction beams, aspheric HOEs represent a much larger class of optical elements than conventional HOEs. It is expected that with these additional degrees of freedom, aspheric HOEs will generally be capable of improved performance in imaging applications as compared to conventional HOEs.

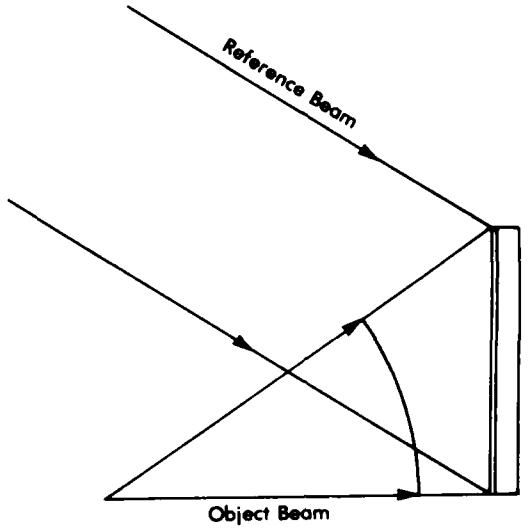


(a) Conventional Holographic Optical Element With a Spherical Object Beam

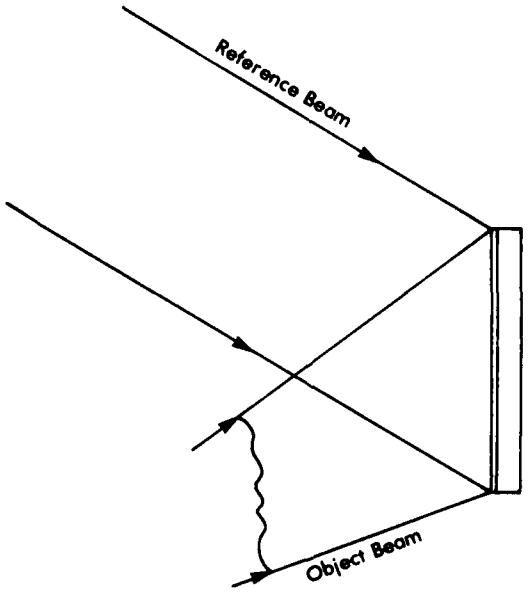


(b) Aspheric Holographic Optical Element With an Aspheric Object Beam

**Figure 1. Construction Configuration of Conventional and Aspheric Holographic Optical Elements**

## 1. GEOMETRIC CONSIDERATIONS

Consider for the moment a HOE which is recorded as shown in Figure 2a and which is read out as in Figure 2b. Here we have assumed that the hologram itself is the entrance pupil of the system. In addition, we assume that the element is operated over a collection of field angles (i.e., the reconstruction wavefront impinges upon the hologram over a range of angles and correspondingly produces image wavefronts over a range of angles). J.R. Fienup has shown [3] that the hologram phase $\phi(x)$ which minimizes the weighted mean-squared phase error is

$$\phi(x) = \left( \sum_{n=1}^{N} W_n \right)^{-1} \sum_{n=1}^{N} W_n \phi_n(x) \tag{1}$$

where $\phi_n$ is the ideal function at field angle n and $W_n$ is its corresponding weighting function. The hologram phase is the difference of the construction wavefront phases

$$\phi(x) = \phi_O(x) - \phi_R(x) \tag{2}$$

where $\phi_O(x)$ is the object wavefront phase and $\phi_R(x)$ is the reference wavefront phase. Conceivably, the reference wavefront, $\phi_R(x)$, could be chosen to be a wavefront which is readily generated, such as a spherical wavefront, and then the object wavefront, $\phi_O(x)$, could be computed using Eq. (2) to produce the desired hologram phase $\phi(x)$. It should be noted, however, that the choice of $\phi_R(x)$ is not totally arbitrary. In general, any realizable phase function must obey the following inequality,

$$\sqrt{\left(\frac{\partial \phi}{\partial x}\right)^2 + \left(\frac{\partial \phi}{\partial y}\right)^2} \leq \frac{2\pi}{\lambda} \tag{3}$$

in order that it may represent a propagating wavefront of wavelength $\lambda$. Violation of this inequality implies that the wavefront is

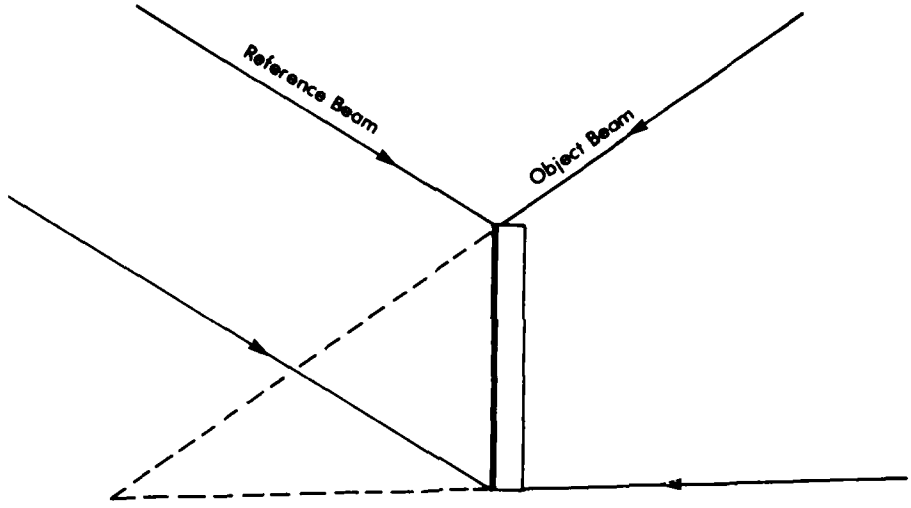


(a) Construction

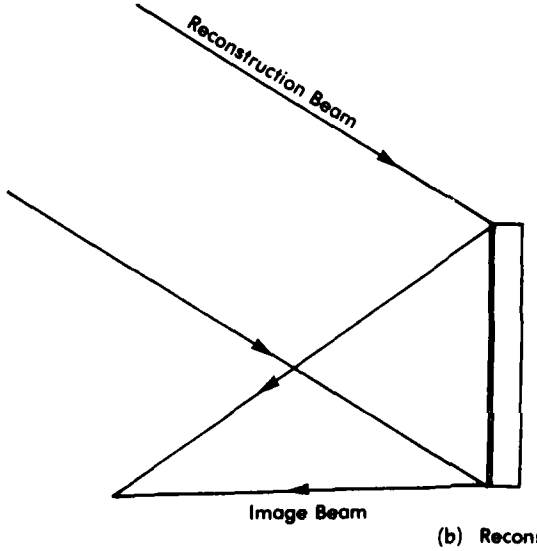


(b) Reconstruction

**Figure 2. Construction and Reconstruction Configuration of a Conventional Reflection Holographic Element**

evanescent. Both $\phi_o(x)$ and $\phi_R(x)$ must satisfy inequality (3). This implies that

$$\left| \frac{\partial \phi_o}{\partial x} \right| = \left| \frac{\partial \phi}{\partial x} - \frac{\partial \phi_R}{\partial x} \right| \leq \frac{2\pi}{\lambda} \tag{4}$$

must also be satisfied. Depending upon the values of $\partial\phi/\partial x$, this may constrain the values of $\partial\phi_R/\partial x$ that the reference wavefront, $\phi_R(x)$, may have.

The direction cosines which describe the direction of propagation of a wavefront ray may be derived from a knowledge of the phase of the wavefront on a plane surface as follows:

$$\ell = \frac{\lambda}{2\pi} \frac{\partial \phi}{\partial x} \tag{5}$$

$$m = \frac{\lambda}{2\pi} \frac{\partial \phi}{\partial y} \tag{6}$$

$$n = \pm(1 - \ell^2 - m^2)^{1/2} \tag{7}$$

where $\ell$, m, n are the x, y, z direction cosines, respectively.

In terms of Eqs. (1) and (2), the hologram phase has an x direction cosine

$$\ell = \frac{\lambda}{2\pi} \frac{\partial \phi}{\partial x} = \frac{\lambda}{2\pi} \left( \sum_{n=1}^{N} W_n \right)^{-1} \sum_{n=1}^{N} W_n \frac{\partial \phi_n}{\partial x}(x) \tag{8}$$

or

$$\ell = \frac{\lambda}{2\pi} \left( \sum_{n=1}^{N} W_n \right)^{-1} \sum_{n=1}^{N} W_n \frac{\partial \phi_o}{\partial x} - \frac{\partial \phi_R}{\partial x} \tag{9}$$

In other words, if we think of the hologram phase as representing a propagating wavefront, we see that its x direction cosine is just

the weighted average of the difference of the direction cosines of the recording wavefronts.

## 2. ENTRANCE PUPIL IN FRONT OF HOE

Next, we consider readout in the case for which the entrance pupil is in front of the HOE as depicted in Figure 3. Intuition would tell us that this geometry is capable of greater performance over extended fields-of-view because at the extreme field angles, the readout wavefront illuminates totally different sections of the hologram. By appropriately recording the hologram in these different sections, the readout geometry may more closely correspond to the recording geometry and thus better performance may be achieved. Another way of looking at this is as follows. At each position x on the hologram, a phase equal to the weighted average of the difference of the recording wavefront phases is recorded. The RMS error of the average phase will be proportional to the ray direction errors (aberrations) upon readout at various field angles. In general, the larger the range of field angles which illuminate hologram position x, the larger will be the RMS error. For the case of the stop located at any position other than at the hologram plane, the range of field angles which illuminate hologram position x will be less than the total field of view of the system and thus the RMS error will be reduced.

Let us now state what this means in terms of Eq. (1). We still want Eq. (1) to be satisfied at each hologram position x; now, however, the range of field angles over which the summation is computed is a function of the hologram position, x. This field angle dependence on x can be conveniently incorporated into the weighting function.

Assume the readout geometry of Figure 3 with an entrance pupil of extent $x_p$ oriented parallel to the hologram and illuminated by

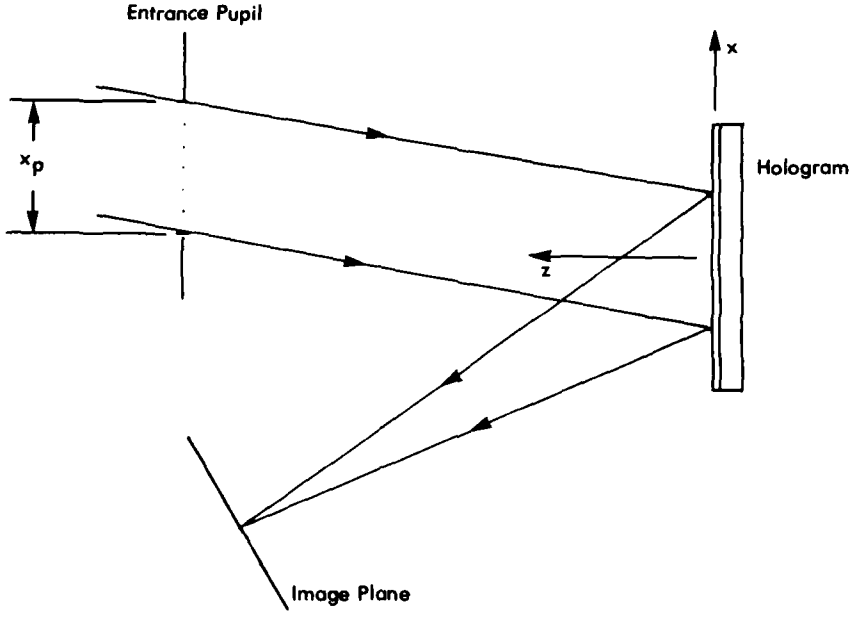


Figure 3. Holographic Reflection Element With Entrance Pupil in Front of the Element

plane waves over an extended field of view. Consider a ray beginning at the center of the entrance pupil and intercepting the hologram at $x_f$. This defines a field angle in terms of its hologram intercept. For each field angle, we can define a hologram phase as a function of hologram coordinate. This corresponds to the difference between the phases of the readout wavefront at the specified field angle and its corresponding desired image wavefront. Thus, the hologram phase may be described as a two-dimensional function of field angle (as specified by hologram intercept) and hologram coordinate,

$$\phi_h = \phi_h(x_f, x) \tag{10}$$

where $x_f$ and $x$ are the field angle intercept and hologram coordinate, respectively. If we now also define a weighting function, $W(x)$, such that

$$W(x) = 0 \text{ for } \left| x \right| > \frac{x_p}{2} \tag{11}$$

and

$$\int_{-\infty}^{\infty} W(x)\, dx = 1 \tag{12}$$

then we can define the composite hologram phase as

$$\phi(x) = \int_{-\infty}^{\infty} W(x - x_f)\phi_h(x_f, x)\, dx_f \tag{13}$$

Once the composite hologram phase of Eq. (13) is determined, perhaps numerically, the task remains as before to choose object and reference wavefronts to realize this phase.

The analysis we have performed to this point has assumed a thin hologram structure. In particular, the efficiency of the diffracted wavefront is not considered. In light of the fact that most practical applications will involve thick holograms, Bragg diffraction

effects must be considered. The following section considers an alternate approach to the diffraction analysis which includes Bragg diffraction requirements.

## 3. VECTOR ANALYSIS OF HOLOGRAPHIC IMAGING

An alternate approach to analyzing the diffraction of a holographic grating is through a vector analysis as described by Spencer and Murty [4] and by Welford [5]. This technique is used extensively in hologram ray tracing programs, including HOAD.

Let the reconstruction and image wavefronts be described at any position by rays perpendicular to the wavefronts in the direction of propagation. Let the rays, in turn, be described by unit vectors, $\vec{C}$ and $\vec{I}$ in a cartesian coordinate space. The components of the unit vectors are simply the direction cosines, i.e.,

$$\vec{C} = \ell_C \hat{x} + m_C \hat{y} + n_C \hat{z} \tag{14}$$

and

$$\vec{I} = \ell_I \hat{x} + m_I \hat{y} + n_I \hat{z} \tag{15}$$

where $\hat{x}$, $\hat{y}$ and $\hat{z}$ are unit vectors forming a right-handed coordinate system such that $\hat{x} \times \hat{y} = \hat{z}$. In addition, let the grating be described by its surface period (fringe spacing), $d_s$ and orientation, $\hat{q}$, where $\hat{q}$ is a unit vector parallel to the fringes that lies in the plane of the surface. Then the following relationship holds

$$(\vec{I} - \vec{C}) \times \hat{n} = (\lambda_C / d_s)\hat{q} \tag{16}$$

where $\hat{n}$ is a unit vector normal to the surface and $\lambda_C$ is the reconstruction free-space wavelength.

Let us now assume that the grating was recorded interferometrically by two wavefronts described by vectors $\vec{O}$ and $\vec{R}$. The recording

grating will have fringe planes with orientation and separation as follows,

$$\vec{G} = \vec{O} - \vec{R} \tag{17}$$

$$d_G = \frac{\lambda_o}{|\vec{G}|} \tag{18}$$

where $\vec{G}$ is a vector normal to the fringe plane, $d_G$ is the fringe plane spacing, and $\lambda_o$ is the construction free-space wavelength. The grating vector component which is parallel to the fringes and lies in the surface tangent plane is given by

$$\vec{Q} = (\vec{O} - \vec{R}) \times \hat{n}$$

and thus, the corresponding surface grating spacing is

$$d_s = \frac{\lambda_o}{|\vec{Q}|} = \frac{\lambda_o}{|(\vec{O} - \vec{R}) \times \hat{n}|} \tag{19}$$

Combining Eqs. (16) and (19), we find

$$(\vec{I} - \vec{C}) \times \hat{n} = \frac{\lambda_c}{\lambda_o} |(\vec{O} - \vec{R}) \times \hat{n}| \hat{q} \tag{20}$$

but

$$\hat{q} = \frac{(\vec{O} - \vec{R}) \times \hat{n}}{|(\vec{O} - \vec{R}) \times \hat{n}|} \tag{21}$$

so

$$(\vec{I} - \vec{C}) \times \hat{n} = \frac{\lambda_c}{\lambda_o} (\vec{O} - \vec{R}) \times \hat{n} \tag{22}$$

This is the standard vector ray tracing equation for holographic gratings used by many ray tracing design programs.

## 4. BRAGG EFFICIENCY CONSIDERATIONS

Equation (22) describes the geometric relationship between the holographic recording and readout wavefronts. The amplitude of the image wavefront, however, is a complex function of the recording geometry, readout geometry and material properties [6]. It is sufficient for the purposes of this analysis, however, to note that for peak efficiency, the Bragg condition is satisfied when the recording grating structure is identical in fringe spacing and orientation to that which would be recorded by the desired readout wavefronts. In equation form, we require that

$$\frac{\lambda_O}{|\vec{O} - \vec{R}|} = d_G = \frac{\lambda_C}{|\vec{I} - \vec{C}|} \tag{23}$$

and

$$\frac{\vec{O} - \vec{R}}{|\vec{O} - \vec{R}|} = \hat{g} = \frac{\vec{I} - \vec{C}}{|\vec{I} - \vec{C}|} \tag{24}$$

where $d_G$ is the fringe spacing and g is a unit vector perpendicular to the fringe planes. The above two equations define orthogonal measures and so we may combine them into a single equation

$$\frac{\hat{g}}{d_G} = \frac{\vec{O} - \vec{R}}{|\vec{O} - \vec{R}|} \cdot \frac{|\vec{O} - \vec{R}|}{\lambda_O} = \frac{\vec{I} - \vec{C}}{|\vec{I} - \vec{C}|} \cdot \frac{|\vec{I} - \vec{C}|}{\lambda_C} \tag{25}$$

or finally

$$\vec{O} - \vec{R} = \frac{\lambda_O}{\lambda_C} (\vec{I} - \vec{C}) \tag{26}$$

This is the vector Bragg constraint which must be satisfied to achieve maximum diffraction efficiency with the desired imaging properties.

It is interesting to compare the imaging Eq. (22) with the combination Bragg and imaging Eq. (26) just developed. Equation (22) is identical to Eq. (26) except that both sides of Eq. (22) are crossed with the surface normal, n. In geometric terms, Eq. (22) relates the wavefront components in the tangent plane of the surface, whereas Eq. (26) relates the wavefronts in a volumetric sense. Alternatively, we may say that Eq. (26) considers the grating structure within the volume of the hologram, whereas Eq. (22) considers the grating structure only upon the surface of the hologram. It follows algebraically that if Eq. (26) is satisfied, then Eq. (22) is satisfied also.

## 5. REALIZABLE WAVEFRONTS

As stated previously, any two-dimensional phase function on a plane $\phi(x,y)$, describes a realizable wavefront, provided the phase does not vary too rapidly in comparison to the propagation constant (see inequality (3)). It also follows that given a phase function which satisfies inequality (3), the ray direction cosines at any point on the wavefront may be computed from the partial derivatives of the phase function as described in Eqs. (5) - (7). From a purely mathematical standpoint, we require that the function $\phi(x,y)$ be both continuous and differentiable. Obviously, two-dimensional polynomial functions satisfy both of these mathematical constraints and are easily differentiated algebraically. Other functions, such as weighted sums of phase functions, may also satisfy the continuity and differentiability constraints, but may require numerical methods to approximate the partial derivatives. In this manner, analytically defined wavefronts can be described as phase functions and ray tracing methods may be used (as in HOAD) to analyze the performance of such a HOE in an optical system.

We now consider the inverse problem, i.e., given two functions (each two-dimensional) which represent the partial derivatives of a

phase function defined on a plane, how do we recover the phase function and perhaps, more importantly, how do we make sure that the phase function is realizable. From vector integral calculus [7], we find that

$$\phi(x,y) = c\int_{(0,0)}^{(x,y)} \frac{\partial\phi}{\partial x}\,dx + \frac{\partial\phi}{\partial y}\,dy \tag{27}$$

provided the line integral is independent of path. In other words, if the two-dimensional funtions, $\partial\phi/\partial x$ and $\partial\phi/\partial y$, are such that the integral of Eq. (27) has the same value regardless of the path of integration from (0,0) to (x,y), then $\phi(x,y)$ is single valued and in fact $\partial\phi/\partial x$ and $\partial\phi/\partial y$ are the partial derivatives of $\phi(x,y)$. Inde-pendence of path, however, is not a property which can be numerically verified, so we need some other method. Fortunately, a second theorem of vector integral calculus provides an answer. It states that if $\partial\phi/\partial x$ and $\partial\phi/\partial y$ have continuous derivatives in a simply connected domain and if

$$\frac{\partial^2\phi}{\partial y\partial x} = \frac{\partial^2\phi}{\partial x\partial y} \text{ or } \frac{\partial \ell}{\partial y} = \frac{\partial m}{\partial x} \tag{28}$$

then the integral of Eq. (27) will be independent of path. The requirement that the derivatives be continuous is a reasonable one since the derivatives are proportional to the ray direction cosines which must vary in a smooth manner for any reasonable wavefront. In general, we consider only simply connected domains (i.e., we do not allow holes within the area of the hologram).

Thus, if the direction cosines (or $\partial\phi/\partial x$ and $\partial\phi/\partial y$) are chosen such that Eq. (28) is satisfied, then Eq. (27) may be used to determine the corresponding two-dimensional phase function. Ultimately, it is the phase function that we want in order to synthesize a computer generated hologram that will produce the desired wavefront.

At this point, we make some observations which may be useful later. First, if we have two realizable phase functions, $\phi_1(x,y)$

and $\phi_2(x,y)$, then any linear combination of these phase functions is also a realizable phase function, because the integration of Eq. (27) is a linear operation. For example, $\phi_3(x,y) = \phi_1(x,y) - 2\phi_2(x,y)$ is a realizable phase function. In a similar manner, if we have two sets of direction cosines which satisfy Eq. (28), then any linear combination of the sets will also satisfy Eq. (28), because the derivatives in Eq. (28) are linear operations. This means that the linear combination may be used in Eq. (27) to arrive at a valid combination phase function. For example,

$$\ell_3 = \ell_1 - 2\ell_2 \qquad m_3 = m_1 - 2m_2 \tag{29}$$

will satisfy Eq. (28) provided $\ell_1$, $m_1$ and $\ell_2$, $m_2$ satisfy Eq. (28) separately.

The final observation we wish to make is that general two-dimensional polynomials, such as,

$$\phi(x,y) = \sum_{i=0}^{m} \sum_{j=0}^{n} a_{ij} x^i y^j \tag{30}$$

are realizable phase functions, as are all linear combinations of such polynomials. Furthermore, any polynomial pairs which satisfy Eq. (28) also can be used with Eq. (27) to obtain a realizable phase function. For example, suppose we have

$$\ell = 2x + y \qquad m = x + 2y \tag{31}$$

Then

$$\frac{\partial \ell}{\partial y} = 1 = \frac{\partial m}{\partial x} \tag{32}$$

and

$$\phi(x,y) = {}_C\int_{0,0}^{x,y} \frac{2\pi}{\lambda} [\ \ell dx + m\ dy] \tag{33}$$

## 6. IMPLEMENTATION

We will now specify a method whereby Eq. (26) may be used to determine the recording wavefronts to obtain the desired performance. We first break Eq. (26) into its components,

$$\ell_o - \ell_R = \frac{\lambda_o}{\lambda_c} (\ell_I - \ell_c) \tag{34}$$

$$m_o - m_R = \frac{\lambda_o}{\lambda_c} (m_I - m_c) \tag{35}$$

$$n_o - n_R = \frac{\lambda_o}{\lambda_c} (n_I - n_c) \tag{36}$$

Presumably, we know what $\ell_I$, $m_I$, $n_I$, $\ell_c$, $n_c$, $\lambda_o$ and $\lambda_c$ are desired to be (as functions of the hologram coordinates, x and y). If we are judicious and choose the pairs $\ell_I$, $m_I$ and $\ell_c$, $m_c$ such that Eq. (28) is satisfied for each pair (perhaps by choosing them as appropriate polynomials), then we know that the right-hand sides of Eqs. (34) - (36) will represent a realizable phase function. It then remains to choose the left-hand-side functions such that they are realizable and equal to the right-hand result. One possible method would be to choose $\ell_R$ and $m_R$ such that they represent some known realizable phase function (such as a polynomial) and then by the linearity we spoke of earlier, $\ell_o$ and $m_o$ will automatically represent a realizable phase function. This method, however, removes some degrees of freedom from the problem. The result may be that the recording beams $\vec{O}$ and $\vec{R}$ may not be the pair with the lowest space-bandwidth product that could be used. A second possibility is to let

$$\ell_o - \ell_R = \frac{1}{2} \frac{\lambda_o}{\lambda_c} (\ell_I - \ell_c) \tag{37}$$

$$m_o - m_R = \frac{1}{2} \frac{\lambda_o}{\lambda_c} (m_I - m_c) \tag{38}$$

$$n_o - n_R = \frac{1}{2} \frac{\lambda_o}{\lambda_c} (n_I - n_c) \tag{39}$$

in which case $\vec{O}$ and $\vec{R}$ will have equal space bandwidth products.

Finally, once $\vec{O}$ and $\vec{R}$ have been established, it is necessary to evaluate Eq. (27) either algebraically if $\vec{O}$ and $\vec{R}$ are described by an algebraic equation, or numerically if $\vec{O}$ or $\vec{R}$ are described by samples.

## SECTION III
## INITIAL DESIGN INVESTIGATIONS

The objectives of the initial design investigations were to locate the major system components and to establish an aspheric combiner design suitable as a starting point in the subsequent system design.

### 1. INITIAL DESIGN OF THE HUD SYSTEM

The objective of the initial design was to locate the major components of the optical system, and to establish the first-order configuration of the construction beams. We assumed a system configuration of the form shown in Figure 4. The initial design was based on satisfying three conditions. The first was the requirement that the optical system fit into the F-16 cockpit, which constrained the locations of the combiner and fold mirror. The second condition was that the holographic combiner have high diffraction efficiency, which constrained the general location of the construction beams. The third condition on the initial design was that the hologram design control astigmatism to a first order, and where possible, minimize other image aberrations.

#### a. SYSTEM LAYOUT

The major objective of the system layout was the placement of the combiner and fold mirror in the cockpit. This task was governed by the requirements of the optical system and the configuration of the cockpit. The optical system requirements that affected the system layout were the size of the exit pupil (3.0 inches vertical by 4.5 inches horizontal), and the instantaneous and vertical fields-of-view, which we defined as follows.

The instantaneous field-of-view (IFOV) measures 12°V by 20°H; it is measured from the center of the exit pupil and, in the vertical

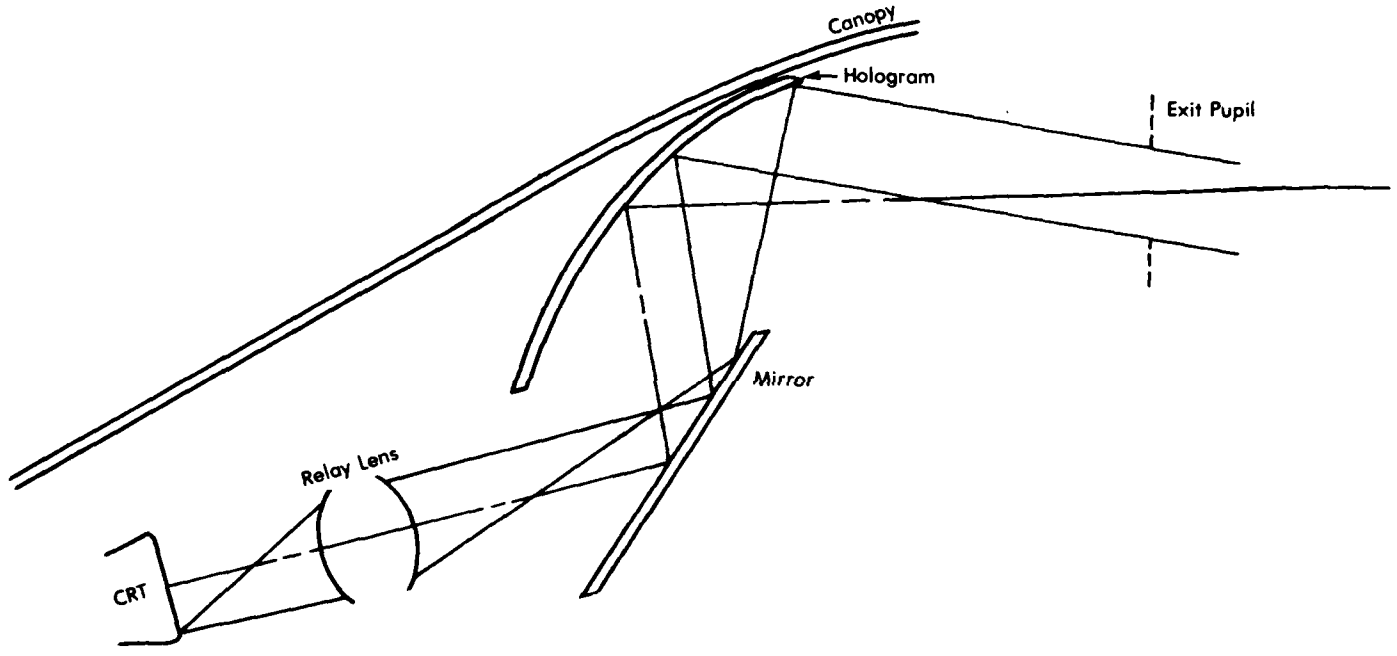


Figure 4. HUD System Configuration

plane, is defined by the horizontal and a ray at an angle of 12° below it. In the horizontal direction, the IFOV is defined by rays at angles of ±10° with the vertical plane.

The total field-of-view (TFOV) is 20°, ± 10° about the center of the field-of-view. In the F-16 cockpit, the TFOV is defined in the vertical plane by a ray from the top of the exit pupil at an angle of 16° below the horizontal and a ray up from the bottom of the exit pupil at a 4° angle. The TFOV is circularly symmetric.

We also define the optical axis to pass through the center of the exit pupil at the center of the fields-of-view; it therefore points downward 6° with respect to the horizontal, toward the nose of the aircraft.

The cockpit boundaries which affect the HUD system, shown in Figure 5, are the following: the windshield clearance line which is located parallel to and 3/4" inside the windshield; the over-the-nose-vision-line (ONVL) which extends down from the center of the exit pupil at 15° from the horizontal; and the ejection line. The combiner could not be placed forward of the windshield clearance line and no part of the system could block the ONVL. We allowed some violation of the ejection line on the grounds that the optical module was sufficiently limited in lateral dimension so as to allow adequate clearance on each side. The optical module as shown in Figure 5 determines boundaries for the fold mirror, relay lens, and CRT.

The combiner was positioned as far forward in the cockpit as was consistent with both the vertical field-of-view requirements and the available space between the windscreen clearance line and the ONVL. The folding mirror, on the other hand, was positioned as far aft as the optical module would allow in order to minimize the angle between the chief ray incident at the center of the hologram before and after diffraction by the hologram, in other words, to minimize the off-axis nature of the hologram.

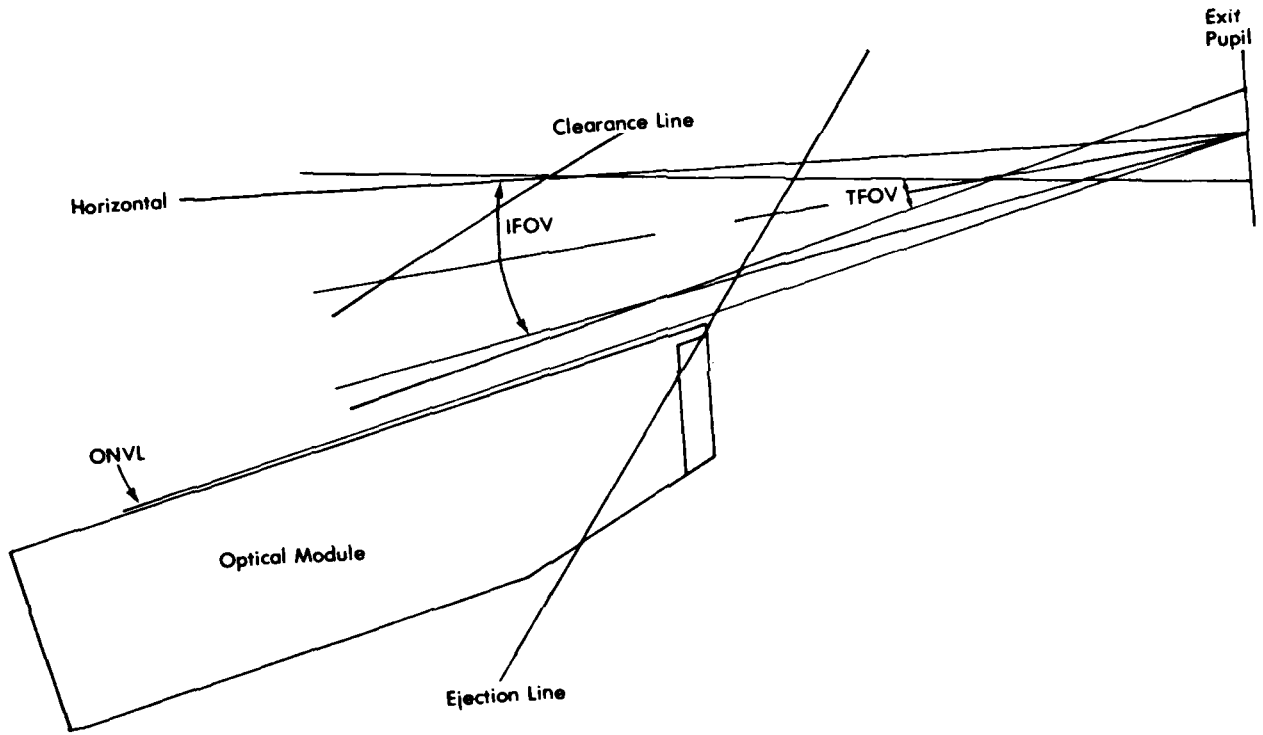


Figure 5. F-16 Cockpit Boundaries and Fields-of-View

The hologram was tilted such that the chief ray incident at the center of the hologram was diffracted at an equal and opposite angle of incidence, as though it had been reflected by classical reflection. This geometry minimized chromatic effects resulting from the spectral bandwidth of the phosphor and tended to minimize distortions arising from asymmetries in the grating geometry.

The size of the hologram was determined by the eye relief, the fields-of-view, the size of the exit pupil, and to some extent, the curvature of the hologram. The size of the folding mirror required to accommodate all rays also depended on these parameters and in addition on the focal length of the hologram, the separation distance between hologram and mirror, and the space allowed by the optical module.

The tilts of the hologram and fold mirror were adjusted so that a ray from the center of the exit pupil in the center of the field-of-view would, after reflection by the fold mirror, be in the approximate center of the optical module parallel to the ONVL.

The relay lens was located 110 mm from the fold mirror, centered between the top and bottom of the optical module. Location of the CRT was put off until the relay lens parameters were defined and until the intermediate image requirements were established.

b. FIRST ORDER COMBINER DESIGN

The objective of the first order combiner design was a conventional holographic combiner design that we could use as a starting place for the aspheric holographic combiner design. Requirements on the first order design were a combiner having high diffraction efficiency over the entire vertical field-of-view and having an image with first order astigmatism corrected. A major factor in the combiner design is the wavelength shift: we assumed a construction wavelength of 514.5 nm and a HUD CRT (reconstruction) wavelength of 544 nm.

The initial combiner design proceeded in two steps. In the first, we assumed spherical construction beams, with parameters chosen to give a reasonable focal length and to satisfy the Bragg condition. In the second step, we added cylindrical lenses to the construction beams to correct first order astigmatism introduced by the hologram.

The configuration of Figure 4 called for a reflection type diffractive element, which is constructed with the point sources of both construction beams lying on the same side of the combiner, with one beam convergent and the other divergent. The requirement that the central ray be diffracted at an angle equal and opposite to its incident angle placed the construction beam point sources on radii making equal and opposite angles with the normal to the hologram at its center (the hologram center was defined to be at the intersection of the optical axis with the combiner).

The radii of the beams, $R_o$ and $R_r$, are related to the focal length of a flat combiner by the equation

$$\frac{1}{f} = \frac{\lambda_c}{\lambda_o}\left(\frac{1}{R_o} + \frac{1}{R_r}\right) \tag{40}$$

where f is the focal length, $\lambda_c$ is the wavelength used during reconstruction and $\lambda_o$ is the wavelength used during recording. The curvature of the combiner also affected its focal length but this was later compensated for by scaling both radii by a suitable amount. The choice of $R_o$ and $R_r$ was based on the first order imaging properties of the HUD optical system. Since the relay lens and the exit pupil are conjugate points with respect to the hologram, reasonable locations for point sources used to form construction beams for holograms were the center of the relay lens and the center of the exit pupil. Although other pairs of conjugate points could have been selected to locate the construction beam point sources, these points were preferable because they are optimum for maintaining a high diffraction efficiency over the field-of-view.

The wavelength shift from 514.5 nm of the laser to 544 nm of the P-43 phosphor required a significant modification of the construction beams in order to satisfy the Bragg condition. At the center of the hologram, we calculated the construction beam angles required to establish fringes with correct spacing such that on reconstruction, the ray incident at the center of the hologram from the center of the exit pupil would satisfy the Bragg condition. The construction beam angles were given by solving

$$\sin \frac{\theta'}{2} = \frac{\lambda'}{\lambda} \sin \frac{\theta}{2} \tag{41}$$

where $\theta$ is the angle between the beams within the hologram medium, and $\lambda$ is the wavelength (in air). If the unprimed quantities refer to the hologram during reconstruction (i.e., in the HUD optical system), then the primed quantities are the corresponding parameters for the hologram construction.

In our design, the ratio

$$\frac{\lambda'}{\lambda} = \frac{0.544}{0.5145} = 1.057$$

For $\theta = 30^\circ$,

then $\theta' = 42.765^\circ$

Since the reference and object wavefronts were spherical, this analysis was correct only at the hologram center; at other locations on the hologram, the construction rays do not make equal and opposite angles with respect to the hologram surface normal. The analysis was sufficient, nevertheless, to locate the construction beams to a first order, leaving refinements to a later step.

The construction beam lengths were also modified to accommodate the wavelength shift. The reference beam length became the distance from the exit pupil to the hologram multiplied by the ratio of reconstruction-to-construction wavelengths. Similarly, the object

beam length was made the distance from the hologram to the relay lens multiplied by the wavelength ratio.

The first step in the combiner design was completed by setting $R_o$ = 300 mm and $R_r$ = 500 mm. As hologram curvature is a useful independent design variable, we chose a substrate radius of 550 mm for the initial design. These parameters resulted in a hologram focal length in the vertical plane of about 223 mm, with approximately 55 mm separating the vertical and horizontal foci.

The second step of the initial combiner design was to add a cylinder lens to each construction beam to correct astigmatism introduced by the hologram. As the initial design was rather preliminary, no attempt was made to find the optimum location and power of the cylinder lenses once the astigmatism had been corrected to a first order.

Figure 6 shows the configuration of the construction beams that resulted from the initial design investigation. One beam is diverging through the construction beam optical system as shown. The other beam is considered to be converging, passing from the combiner through its cylinder lens to a point focus. We design the latter beam by tracing rays from the point source to the hologram, where the ray directions are reversed by the raytrace program. This design resulted in a combiner with a focal length of 193 mm, and which is predicted to maintain over 90 percent diffraction efficiency over the vertical field.

## 2. ASPHERIC COMBINER

The aspheric combiner design was based on the analytical definition of the phase of each construction beam at the hologram. The objective of the combiner design was an aspheric hologram with the correct first order imaging properties, corrected astigmatism, and, if possible, low coma and low distortion. The procedure began by

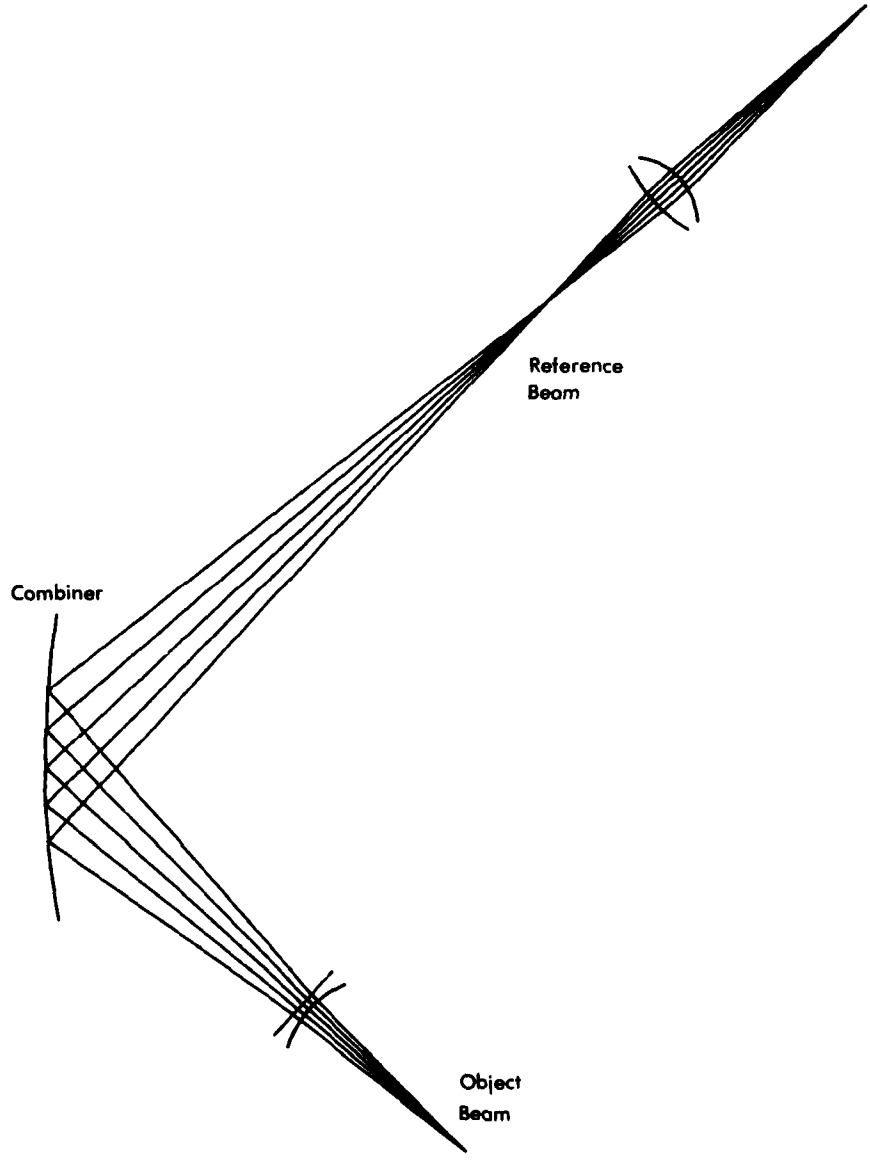


Figure 6. Construction Beam Configuration for Initial Combiner Design

replacing the conventionally-defined, anamorphic construction beams discussed in the previous section with analytically defined construction beams having the approximate forms of the anamorphic wavefronts. We then manually adjusted the parameters defining the construction wavefronts to improve the hologram performance, and finally optimized the construction wavefronts using the optimization routines of the HOAD program [8]. As it turned out, the manual adjustment of the construction wavelength parameters was sufficient to establish a hologram design with which to begin system integration and optimization.

a. ANALYTICALLY DEFINED WAVEFRONTS

In all of our investigations, the phase $\phi(x,y)$ of each construction beam at the hologram was defined in terms of an expansion in Legendre polynomials, expressed as

$$\phi(x,y) = \sum_{i=0}^{9} \sum_{j=0}^{9} C_{ij} L_i(x_r) L_j(y_r) \tag{42}$$

in which $x_r$ and $y_r$ are the relative coordinates

$$x_r = \frac{2x}{D} \ , \ y_r = \frac{2y}{D}$$

where x and y correspond to vertical and horizontal coordinates of the hologram, respectively, $C_{ij}$ are coefficient weighting values specified by the user, and D is the hologram diameter. Legendre polynomials are attractive because they are orthogonal, which means that changing the coefficient of one polynomial does not affect the weighting of the other polynomials. Some examples of Legendre polynomials are given below.

$$L_1(x) = x \tag{43a}$$

$$L_2(x) = \frac{1}{2}(3x^2 - 1) \tag{43b}$$

$$L_3(x) = \frac{1}{2}(5x^3 - 3x) \tag{43c}$$

$$L_4(x) = \frac{1}{8}(35x^4 - 30x^2 + 3) \tag{43d}$$

Notice that the magnitude of the polynomial is unity when $x = \pm 1$, with the sign of the polynomial at $x = -1$ depending on the order of the polynomial. It is because of this property that we used relative hologram coordinates in Eq. (42).

As an example of the use of the Legendre polynomial expansion to describe a wavefront, let us consider the case of a spherical wavefront. We assume the geometry shown in Figure 7, with the hologram in the x-y plane, illuminated by a spherical wave diverging from the point $x_0$, 0, $z_0$ located a distance R from the center of the hologram. The phase $\phi(x,y)$ of the wavefront at the hologram to fourth order is expressed as

$$\begin{aligned}\phi(x,y) = {} & C_{10}L_1(x_r) \\ & + C_{20}L_2(x_r) + C_{02}L_2(y_r) \\ & + C_{12}L_1(x_r)L_2(y_r) + C_{30}L_3(x_r) \\ & + C_{40}L_4(x_r) + C_{22}L_2(x_r)L_2(y_r) + C_{04}L_4(y_r)\end{aligned} \tag{44}$$

where, again,

$$x_r = \frac{2x}{D}\ ,\ y_r = \frac{2y}{D}$$

The coefficients are given by

$$C_{10} = -\frac{Dx_0}{2\lambda R} + \frac{C_{12}}{2} + \frac{3C_{30}}{2} \tag{45a}$$

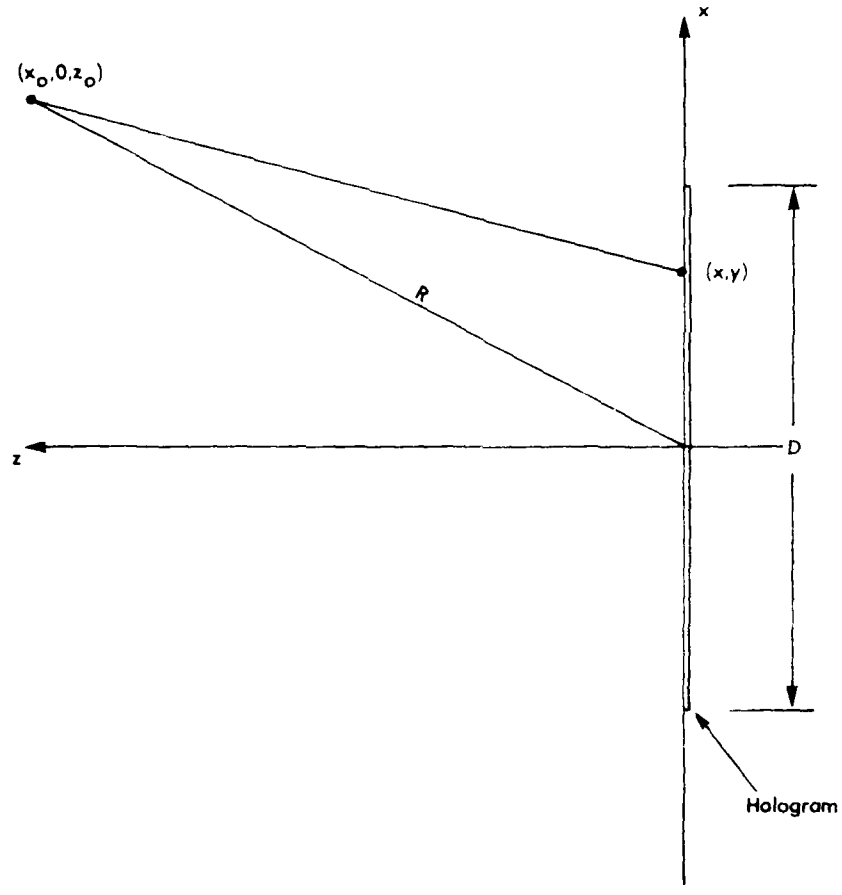


Figure 7. Geometry Used to Describe Analytically Defined Wavefronts

$$C_{20} = \frac{D^2}{12\lambda R}\left[1 - \left(\frac{x_o}{R}\right)^2\right] + \frac{C_{22}}{2} + \frac{15C_{40}}{6} \qquad (45b)$$

$$C_{02} = \frac{D^2}{12\lambda R} + \frac{C_{22}}{2} + \frac{15C_{40}}{6} \qquad (45c)$$

$$C_{12} = \frac{D^3 x_o}{24\lambda R^3} \qquad (45d)$$

$$C_{30} = \frac{D^3 x_o}{40\lambda R^3}\left[1 - \left(\frac{x_o}{R}\right)^2\right] \qquad (45e)$$

$$C_{40} = \frac{-D^4}{560\lambda R^3}\left[1 - 6\left(\frac{x_o}{R}\right)^2 + 5\left(\frac{x_o}{R}\right)^4\right] \qquad (45f)$$

$$C_{22} = \frac{D^4}{288\lambda R^3}\left[\left(\frac{x_o}{R}\right)^2 - 2\right] \qquad (45g)$$

$$C_{04} = \frac{-D^4}{560\lambda R^3} \qquad (45h)$$

with

$$R = \left(x_o^2 + y_o^2\right)^{1/2}$$

b. DESIGN OF THE ASPHERIC COMBINER

The aspheric combiner design began by establishing a Legendre polynomial expansion that approximated the anamorphic wavefronts previously designed, as these were known to represent reasonable starting points for combiner design optimization. We used the fourth-order expansion outlined in the previous section to establish a spherical wave that diverged from (or converged to) the vertical

point focus for each construction wavefront. Because we assumed a curved hologram substrate (with a radius of curvature of 550 mm), the fourth-order expansion, which was derived for flat holograms, did not result in a combiner with the desired focal length. Therefore, working with one wavefront at a time, we scaled $x_o$ and $z_o$ to adjust the coefficients in Eq. (45) until the vertical focal length of the hologram (191 mm) was the same as that of the conventional holographic combiner described in Section III.1.

The resulting combiner had the desired focal length, but required an intermediate image with large amounts of tilt and astigmatism. We found that manual adjustment of certain weighting coefficients was effective in improving different aspects of the hologram performance. For example, the primary curvature of each construction wavefront is controlled by the second-order weighting coefficients $C_{20}$ and $C_{02}$, which determine the strength of the $x^2$ and $y^2$ phase variations, respectively. These coefficients were therefore effective at correcting the hologram astigmatism. Similarly, we observed that the $C_{30}$ coefficient was useful for adjusting the tilt required of the image surface over the vertical field whereas $C_{40}$ was effective in adjusting the curvature required of the image surface over the vertical field. Because of the symmetry of the optical system in the horizontal, or y, direction, the set of available coefficients was limited to those that weighted polynomials that were even in y, such as $C_{10}$, $C_{12}$, $C_{14}$, $C_{16}$, etc.

We found that by careful adjustment of the coefficients, we were able to establish construction beam wavefronts that resulted in good hologram performance. The tilt required of the intermediate image surface was reduced and the hologram astigmatism was corrected over most of the field-of-view. The distortion introduced by the hologram was significantly reduced over that of the baseline hologram design of Section III.1. The major remaining aberration introduced by the hologram was coma, with a relatively small amount of spherical aberration.

We completed the aspheric combiner design by a computer optimization of the design that we had arrived at through manual adjustment of the wavefront weighting coefficients. Although we had hoped for considerable reductions in coma, we found that the optimization did not result in significant overall performance improvements of the combiner.

The completed aspheric combiner design had a focal length of 200 mm with construction wavefronts described by defining the wavefront phase on the hologram surface in terms of Legendre polynomials. The weighting coefficients for both wavefronts are given in Table 1. The very small values of several of the reference beam coefficients are not significant. They resulted from the fourth-order expansion used to establish the initial construction beam parameters, and were not changed thereafter. Figures 8 and 9 show ray traces of the reference and object wavefronts, respectively; a considerable amount of anamorphism is apparent in both wavefronts.

c. ASPHERIC COMBINER PERFORMANCE

In the HUD optical system, the relay lens forms an intermediate, real image of the CRT display at the focal surface of the holographic combiner, so that the latter, in turn, will collimate the display illumination. Because of the aberrations and distortions introduced by the hologram, the relay lens must form an intermediate image aberrated and distorted in such a way as to exactly compensate for the degradation caused by the hologram. We can therefore gauge the hologram performance by examining the intermediate image required by the hologram in order to form a high quality image when viewed from the exit pupil. A convenient way to ascertain the intermediate image characteristics is to trace collimated ray bundles at several field angles from the exit pupil to the hologram and determine the image formed by the hologram. The image so formed represents exactly the image that the relay lens will be required to form.

TABLE 1
WEIGHTING COEFFICIENTS FOR ASPHERIC COMBINER
CONSTRUCTION WAVEFRONTS

| Object Beam | | Reference Beam | |
|---|---|---|---|
| $C_{10}$ | -258580.0 | $C_{10}$ | -263890.0 |
| $C_{20}$ | -17417.0 | $C_{20}$ | 1750.0 |
| $C_{30}$ | 6000.0 | $C_{30}$ | 17.0 |
| $C_{40}$ | -2500.0 | $C_{40}$ | 0.123 |
| $C_{02}$ | -39000.0 | $C_{02}$ | 3248.0 |
| $C_{12}$ | 5444.0 | $C_{12}$ | 55.27 |
| $C_{22}$ | 511.6 | $C_{22}$ | -0.523 |
| $C_{04}$ | 3000.0 | $C_{04}$ | -0.175 |
| $C_{24}$ | 3000.0 | | |
| $C_{34}$ | 6000.0 | | |

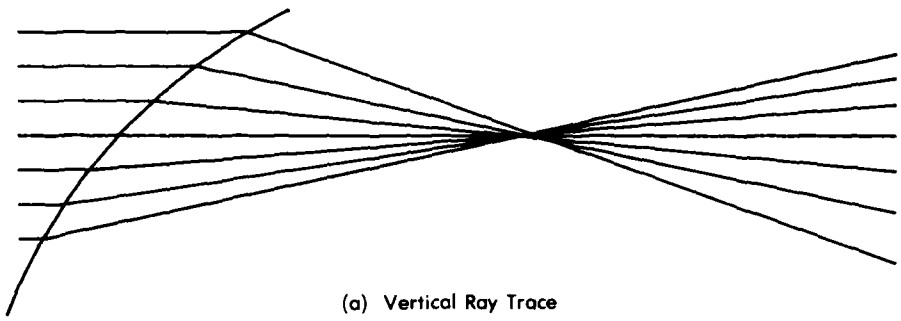

(a) Vertical Ray Trace

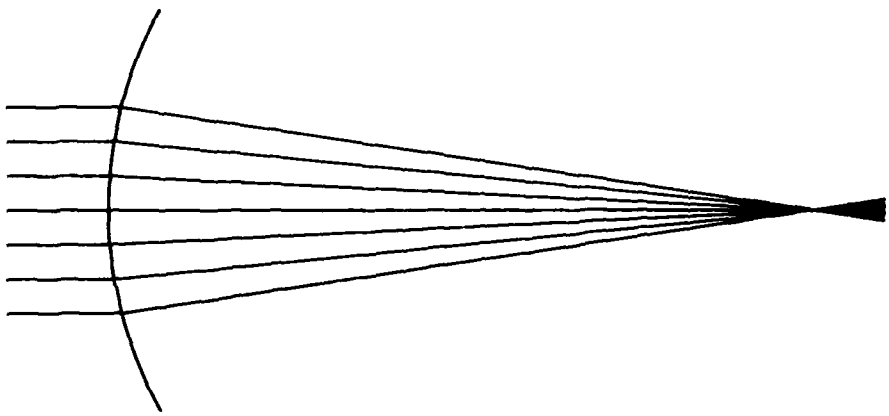

(b) Horizontal Ray Trace

**Figure 8. Ray Traces of the Aspheric Combiner Reference Beam**

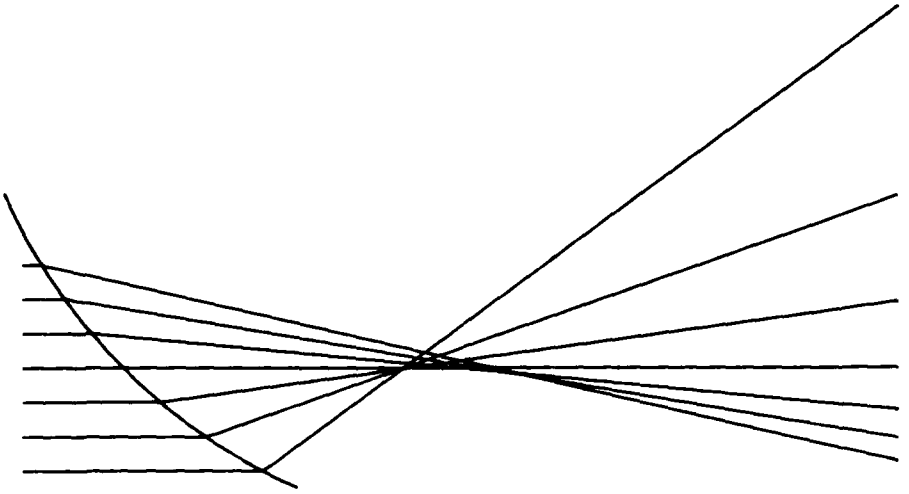

(a) Vertical Ray Trace

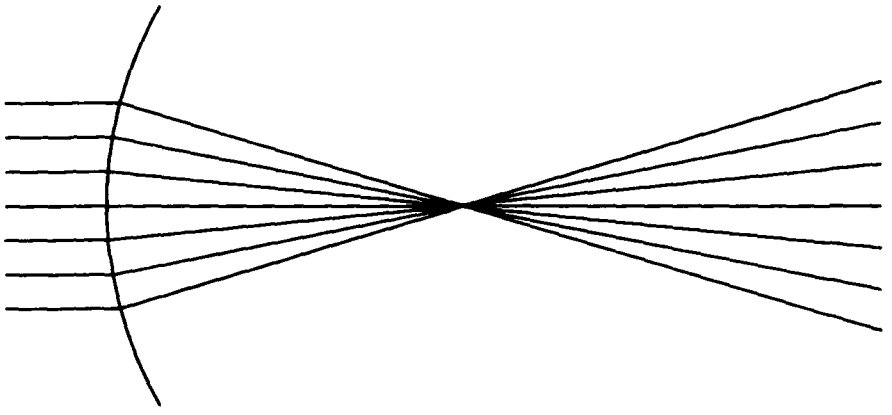

(b) Horizontal Ray Trace

Figure 9. Ray Traces of the Aspheric Combiner Object Beam

To determine the shape and tilt of the intermediate image surface, we traced a small pencil of parallel rays at a number of field angles from the center of the exit pupil to the intermediate image. Figure 10 shows plots of the image locations formed by the ray pencils for both elevation and azimuth variations about the center of the field. In both plots, the horizontal axis is coincident with the optical axis of the system (which coincides with the chief ray in the center of the field-of-view). In the plots, the hologram lies to the left of the image surface, and the labels on the horizontal axis represent distance from the center of the hologram. In Figure 10a, the image surface is tilted by 41° from the vertical, and it is slightly "s"-shaped. The image surface in azimuth is slightly curved, and is convex toward the hologram. The images formed by vertical and horizontal fans are indicated by the two symbol types on the plots; the astigmatism correction is good at most field angles.

We plotted ray intercept curves as shown in Figure 11 to determine the amount and types of aberrations introduced by the combiner. Data for a ray intercept plot are obtained by tracing a fan of parallel rays from the exit pupil to the image formed by the hologram, and at the image plane calculating the x and y (vertical and horizontal) displacements between each ray and the chief ray (the chief ray is the ray that passes through the center of the exit pupil). The image plane intercepts of the individual rays relative to the chief ray intercept are plotted as a function of the intercepts of the rays in the input fan (at the exit pupil of the HUD system). For a perfect image, all points would lie on the horizontal axis as the image plane intercepts would all be zero relative to the chief ray intercept.

Figure 11 shows five sets of ray intercept curves made for five different field angles. At each field angle, two plots are drawn corresponding to vertical and horizontal fans passing through the

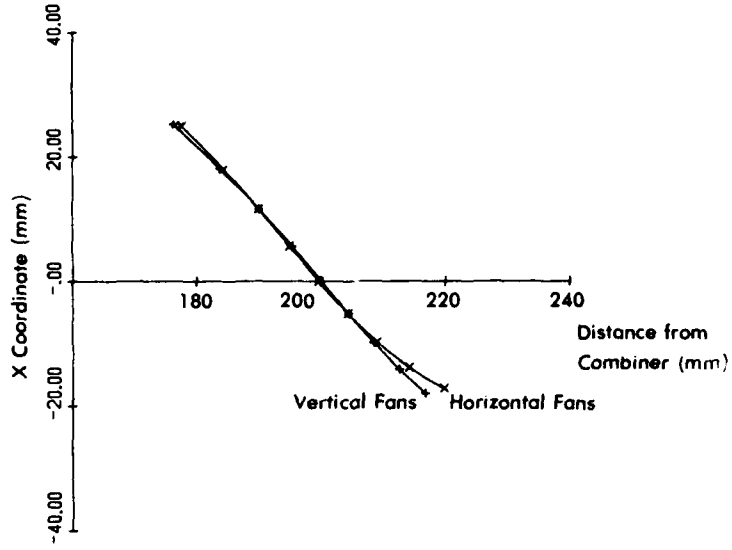


(a) Image Surfaces in the Vertical Plane Formed by Variation of the Vertical Field Angle Over a 12° Field. The Symbols Correspond to an Angular Increment of 2.0°

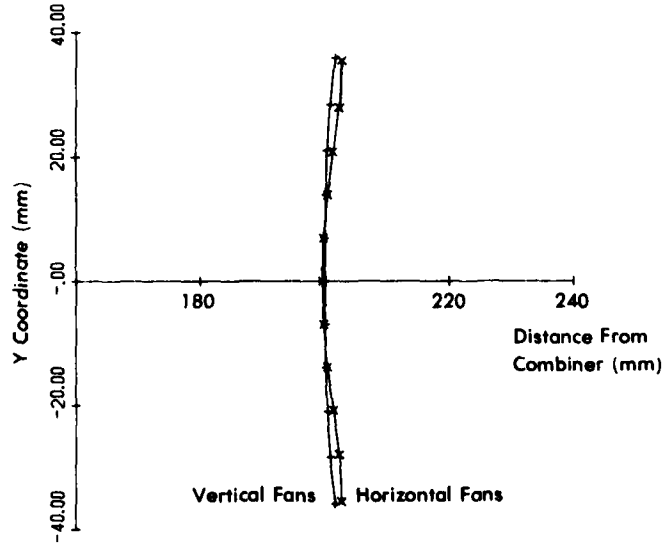


(b) Image Surfaces in the Horizontal Plane Formed by Variation of the Horizontal Field Angle Over a 30° Field. The Symbols Correspond to an Angular Increment of 2.5°

**Figure 10. Image Surfaces Formed by the Aspheric Combiner**

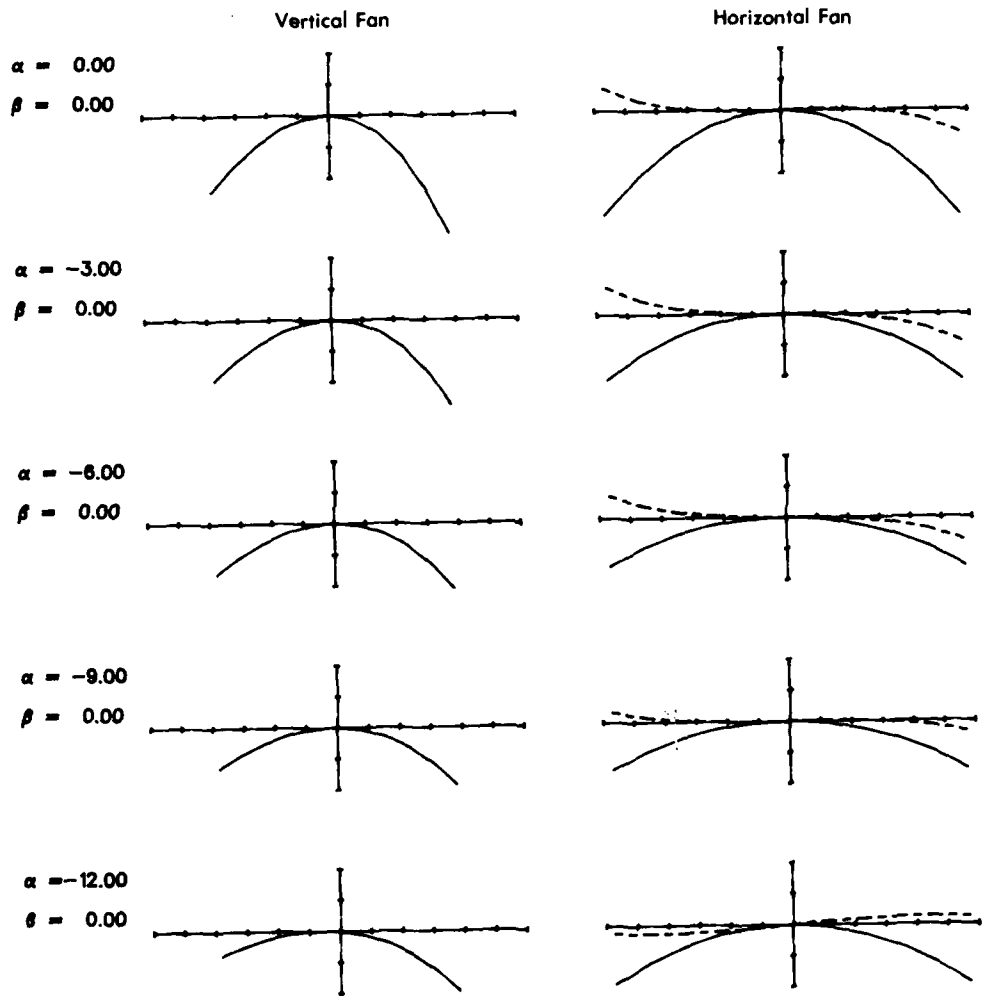


Figure 11. Ray Intercept Curves for the Aspheric Combiner at Five Vertical Field Angles. The distance between tick marks on the horizontal axes is 10 mm; the distance between tick marks on the vertical axes is 1.0 mm.

exit pupil. The tick marks along the vertical axes each represent an interval of 1.0 mm at the image plane whereas the tick marks along the horizontal axes represent intervals of 10 mm in the input fan. The vertical and horizontal input fans usually extend across the vertical and horizontal diameters of the exit pupil, respectively. The curves correspond to elevation angles (denoted by $\alpha$) of 0, -3, -6, -9, and -12°; the azimuth angle in each case is 0°. The solid curves in Figure 11 represent the vertical intercepts of the rays and the dashed curves represent horizontal intercepts. For a hologram with a 200 mm focal length, an intercept of 1 mm corresponds to 5 mr of ray error at the exit pupil.

In Figure 11, the solid curves are generally concave downward, indicating coma in the image. The dashed curves tend to be slightly "s"-shaped, which indicates the presence of spherical aberration. Ray errors at the edges of the exit pupil are on the order of 10 to 15 mr.

To obtain a qualitative measure of distortion, we traced a set of rays from the center of the exit pupil to a plane tangent to the center of the intermediate image surface. The rayset comprised rays distributed uniformly over the instantaneous field-of-view. Figure 12 shows the intercepts of the rayset at the intermediate image plane; keystone distortion is evident with points of constant elevation lying on lines curved upward.

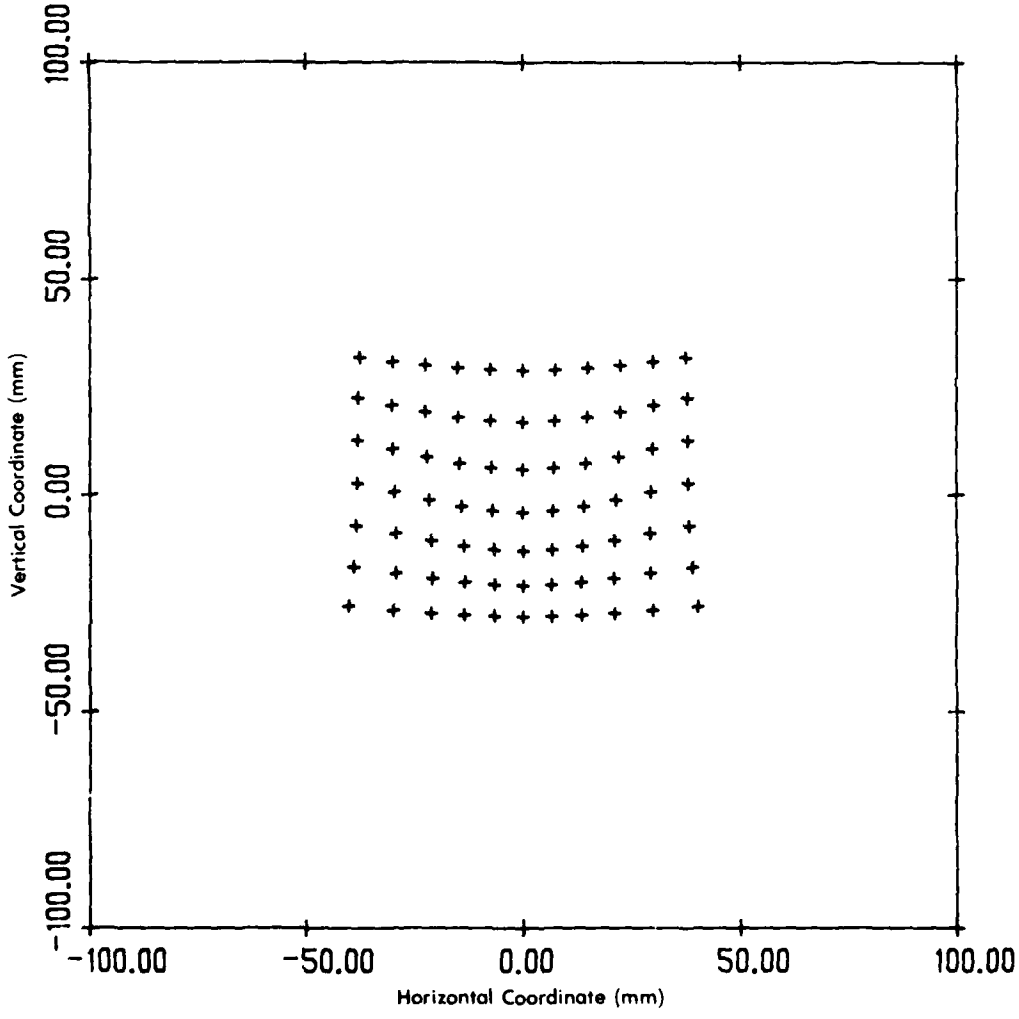


Figure 12. Ray Intercepts Formed by the Aspheric Combiner at the Intermediate Image Plane

# SECTION IV
# SYSTEM DESIGN

The system design involved the addition of the fold mirror, relay lens, and CRT image plane to the aspheric combiner design established previously. Most of the design effort concentrated on computer optimization of the system parameters, with the goal of minimizing aberrations and distortion while maintaining high diffraction efficiency at the combiner.

## 1. SYSTEM COMPONENTS

System components added were the fold mirror, relay lens, CRT image plane, and ultimately, the CRT faceplate. The fold mirror folds the optical path between the F-16 optical module and the combiner. The mirror was made to be slightly convex to reduce the angular spread of the ray bundles between the relay lens and the mirror.

The initial relay lens was in triplet form, and comprised a doublet of positive lens elements (nearest the fold mirror), a single negative element, and a triplet of positive elements. The six elements were initially coaxial, and provided a magnification close to unity.

The CRT image plane was initially located about 85 mm from the nearest surface of the relay lens, and its vertical extent corresponding to the instantaneous vertical field was 37 mm.

## 2. DESIGN PROCEDURE

Because of the large number of parameters describing the system, the design procedure relied on simultaneous multivariable optimization with the HOAD program. The optimization algorithm was based on the damped least squares method that is commonly used in optical design as it is well suited to optimization of nonlinear systems. The

optimization process reduces a merit function that is the sum of the squares of individual system errors or defects.

In our design optimization, the merit function comprised three groups of system defects: ray errors, distortion errors, and efficiency errors. Ray errors, or aberrations, were measured at several exit pupil locations and at several field angles. For each field angle, we traced a set of 5 or 6 parallel rays from the exit pupil to the CRT image plane; the rayset included a chief ray passing through the center of the exit pupil with the remaining rays distributed along the vertical and horizontal centerlines of the exit pupil. The ray errors were calculated as the image plane intercepts of the individual rays relative to the chief ray intercept.

Distortion errors were measured by tracing a set of rays, distributed in field angle over the instantaneous field-of-view, from the center of the exit pupil to the CRT image plane. In a distortion-free system, the rayset would form a rectangular grid at the CRT. The distortion contribution to the merit function was made up of departures of the actual ray intercepts from a perfectly rectangular grid, where the grid spacing was determined as the distance between the rays nearest to the central ray. To simplify the distortion measurements, we compared distances at the CRT that corresponded to equal increments in field angle. Consequently, the optimization was based on satisfying the equation $h = k\theta$ where $h$ is the image height at the CRT, $\theta$ is the field angle at the exit pupil, and $k$ is a constant; both $h$ and $\theta$ are measured relative to the center of the field-of-view. Since we anticipated that the ultimate display source would be a matrix addressed device, for most of our design investigations, we allowed the constant to be different in the horizontal and vertical directions.

Five rays were used to monitor the hologram efficiency, primarily to prevent the design parameters from drifting away from the geometry

required to maintain high diffraction efficiency over both the extent of the exit pupil and the field-of-view. The coupled wave analysis [6] used to calculate the hologram diffraction efficiency is correct only for rays lying in a plane of incidence that also contains the grating vector (a vector that is perpendicular to the grating planes within the hologram medium); in the HUD system, this is the vertical plane lying in the center of aircraft (the xz-plane in our coordinate frame). Consequently, the five rays used to sample the hologram efficiency all lay in the xz-plane. Three rays passed through the center of the exit pupil at the top, center, and bottom of the IFOV (0°, -6°, and -12°, respectively). Of the two additional rays, one passed through the top of the exit pupil at an angle corresponding to the bottom of the TFOV (-16°) and the other passed through the bottom of the exit pupil at the top of the TFOV (+4°). For the efficiency calculations, we assumed a hologram thickness of 10 μm and a refractive index modulation of 0.04.

We changed the rayset occasionally as the design evolved. The initial optimization was performed with rays covering an undersized exit pupil and with coarse sampling for distortion correction. As the design improved, the rayset was redistributed to correspond to the full exit pupil size and rays were added for increased distortion sampling. The rayset used in the final optimization had a total of 77 rays, of which 37 were used to determine ray errors, 45 were used to measure distortion, and 5 were used to measure the hologram efficiency (some rays contributed to more than one error calculation). In addition to changing the rayset, we also altered as appropriate the weighting with which the squares of the individual errors were added to the merit function.

The HUD optical system was described by more than 100 parameters that were reasonable optimization variables. Of these parameters, 64 were construction beam weighting coefficients while most of the remaining variables were associated with the relay lens. Although

we did not optimize with all of the variables at once, we did use most of the variables over the course of the investigation, with a typical optimization run including 25 variables selected from the total set. We found that occasionally adding a new variable (such as a lens decentration or tilt) was effective at increasing the rate of improvement in the optimization results.

## 3. DESIGN RESULTS

Computer optimization was carried out using the HOAD program. The optimization resulted in an aspheric combiner that differed considerably from the initial design and in a relay lens with tilted and decentered elements.

### a. ASPHERIC COMBINER

The resultant aspheric combiner was defined by a greater number of construction beam weighting parameters than had been used in the initial combiner design. As in the initial design, both construction wavefronts were anamorphic; the coma, however, which had been observed in the object beam moved to the reference beam. Ray traces of the reference and object beams are shown in Figures 13 and 14, respectively. In addition, the radius of curvature of the combiner decreased slightly from 550.1 mm to 549.3 mm. The weighting coefficients that define the reference and object beams are shown in Table 2. Whereas a total of 18 coefficients had been used to specify the construction beams of the initial combiner design, the construction beams of the final combiner design utilized a total of 66 coefficients.

The performance of the aspheric combiner is indicated by the ray intercept curves in Figure 15. The coma that was evident in the initial combiner design (Figure 11) was decreased but not eliminated, and some astigmatism has been added. The astigmatism compensates

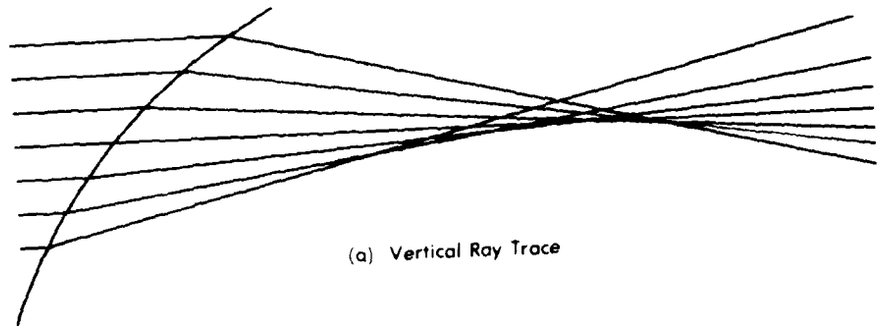

(a) Vertical Ray Trace

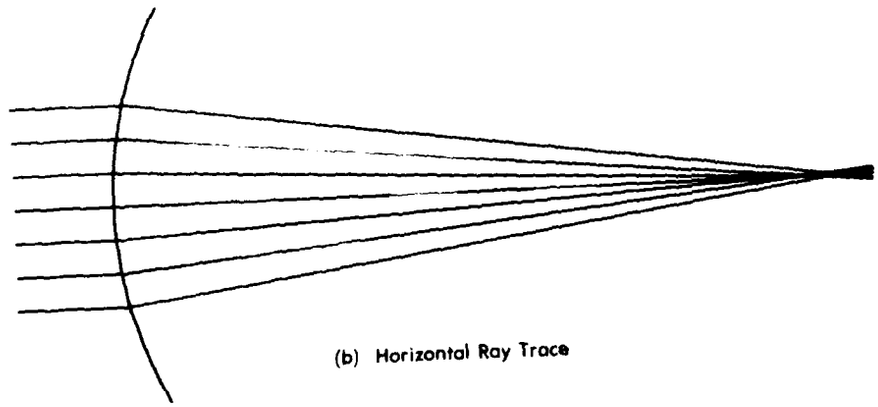

(b) Horizontal Ray Trace

Figure 13. Ray Traces of the Final Aspheric Combiner Reference Beam

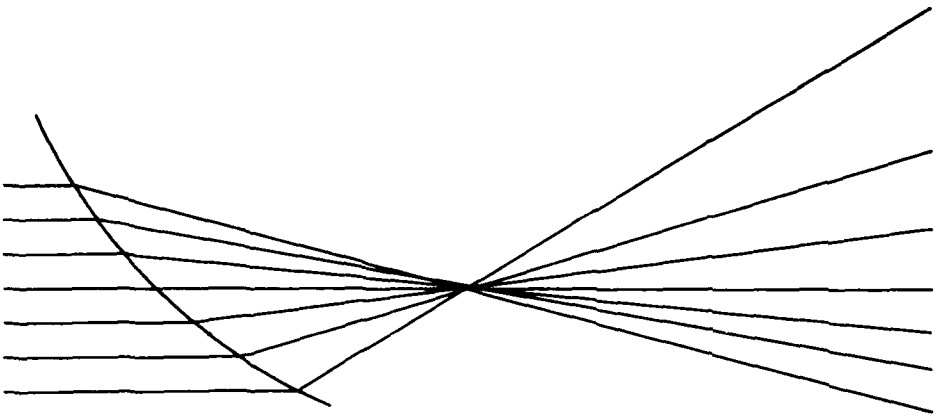

(a) Vertical Ray Trace

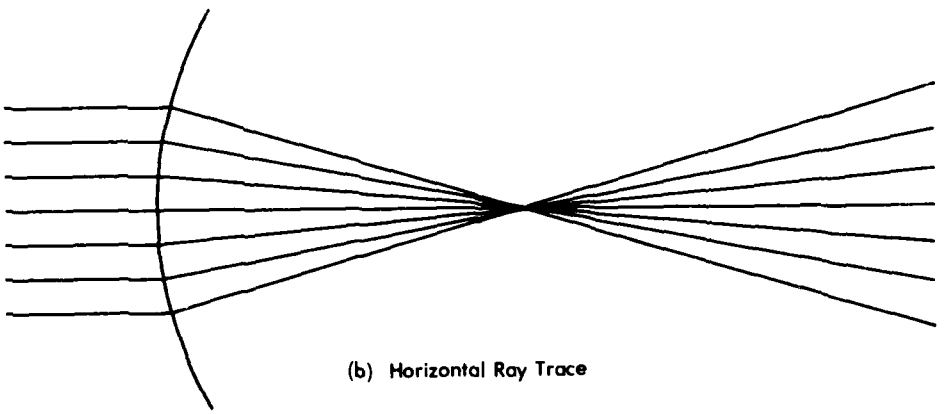

(b) Horizontal Ray Trace

Figure 14. Ray Traces of the Final Aspheric Combiner Object Beam

TABLE 2
WEIGHTING COEFFICIENTS FOR THE FINAL ASPHERIC
COMBINER CONSTRUCTION WAVEFRONTS

Object Beam

| | | | |
|---|---|---|---|
| C10 | -258580.0 | C04 | 150.60 |
| C20 | -9133.5 | C14 | 8776.4 |
| C30 | 4621.4 | C24 | 1622.9 |
| C40 | -1627.9 | C34 | 2711.3 |
| C50 | -301.17 | C44 | 122.31 |
| C60 | -239.70 | | |
| C70 | 620.91 | C06 | 358.37 |
| C80 | 230.79 | C16 | 2383.9 |
| C90 | 526.96 | C26 | -23.742 |
| C02 | -35240.0 | C08 | 62.332 |
| C12 | 31463.0 | C18 | 57.548 |
| C22 | 3310.2 | | |
| C32 | 3618.2 | | |
| C42 | 153.54 | | |
| C52 | -2303.4 | | |
| C62 | -177.46 | | |

Reference Beam

| | | | |
|---|---|---|---|
| C10 | -262889.0 | C04 | -1730.6 |
| C20 | -910.09 | C14 | -1578.0 |
| C30 | -2515.5 | C24 | -180.31 |
| C40 | 752.01 | C34 | -507.19 |
| C50 | -1033.5 | C44 | 146.00 |
| C60 | -417.73 | C54 | -283.96 |
| C70 | -683.85 | C64 | -370.24 |
| C80 | -85.929 | C74 | 354.98 |
| C90 | -316.70 | C84 | -494.25 |
| C02 | -43.005 | C06 | 249.29 |
| C12 | 2863.4 | C16 | -179.36 |
| C22 | 1346.7 | C26 | 55.215 |
| C32 | 6628.0 | C36 | 375.31 |
| C42 | -269.56 | C46 | -365.22 |
| C52 | -68.542 | C56 | 202.08 |
| C62 | -165.57 | C66 | -542.16 |
| C72 | -141.01 | | |
| C82 | -156.42 | C08 | -20.738 |
| C92 | -123.20 | C18 | -299.30 |
| | | C28 | -193.14 |
| | | C38 | -174.55 |
| | | C48 | 10.498 |

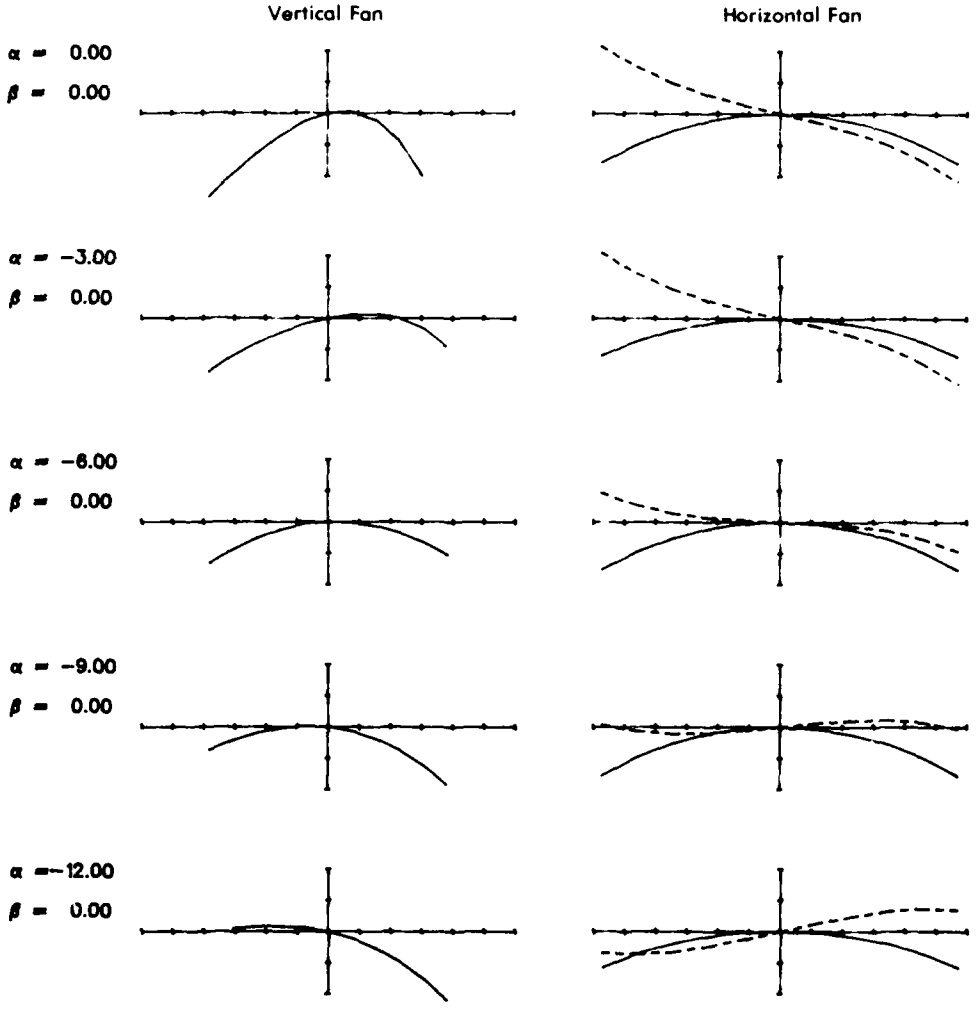


Figure 15. Ray Intercept Curves for the Final Aspheric Combiner at Five Vertical Field Angles. The distance between tick marks on the horizontal axes is 10 mm; the distance between tick marks on the vertical axes is 1.0 mm.

for astigmatism introduced by the tilts and decenters of the relay lens that were required to correct for the coma.

b. RELAY LENS

The relay lens retained its basic triplet form except that during the design optimization, we split the center negative element into two negative elements. In the course of the optimization procedure, one of the negative elements became a positive element, with the second element taking on stronger negative power.

The design of the relay lens proceeded with consideration given to lens manufacture and assembly. All surfaces were kept spherical, and the number of tilts was controlled by arranging the lens elements into three groups.

Figure 16 shows the configuration of the relay lens that resulted from the system optimization. In Figure 16, the broken line connects the vertices of the lens elements and the solid line represents a ray traced from the center of the exit pupil at the central field angle. The lens elements are arranged in three groups that are tilted and decentered with respect to one another. The group nearest the fold mirror is a positive doublet in which both elements are coaxial. The second, or center group, comprises a positive and a negative element which are decentered vertically with respect to each other, but which have parallel axes of rotation. The third group is a positive triplet in which the element nearest to the CRT is decentered vertically with respect to the first two elements; its axis is parallel to the axis of the first two elements.

The relay lens prescription is given by group in Table 3, in which a positive radius of curvature indicates that the center of curvature lies to the left of the surface as shown in Figure 16, and a positive decentration indicates a displacement upward in Figure 16. The figure also indicates the surface and group numbering.

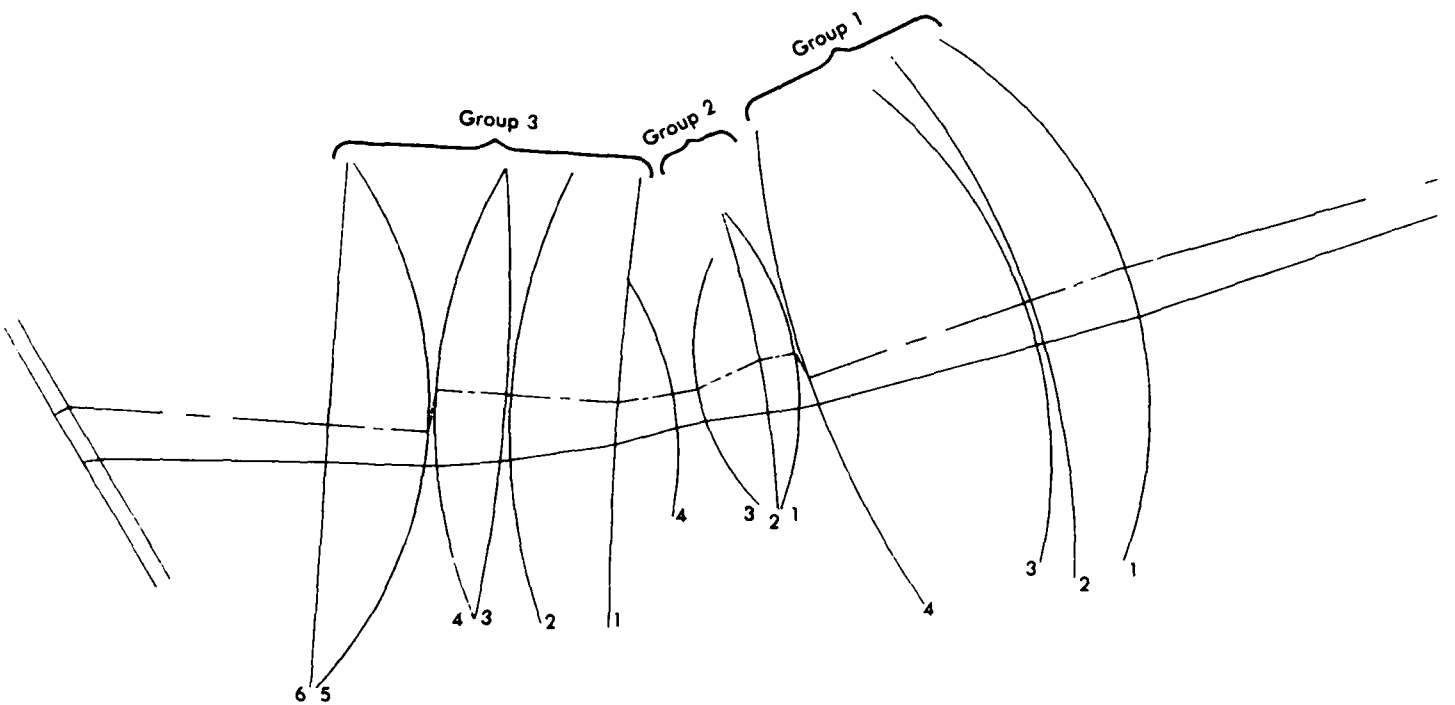


Figure 16. Relay Lens Configuration. The broken line connects the vertices of the lens elements and the solid line represents a ray at the center of the field-of-view

TABLE 3
RELAY LENS PARAMETERS BY GROUP

| Group 1 Surface No. | Glass Type | Index | Thickness (mm) | Radius (mm) | Decentration (mm) |
|---|---|---|---|---|---|
| 1 | LaSF N3 | 1.8127 | 20.000 | 86.461 | |
| 2 | AIR | 1.00 | 1.300 | 154.417 | |
| 3 | BK 7 | 1.5188 | 45.500 | 94.482 | |
| 4 | AIR | 1.00 | | -193.701 | |
| Group 2 | | | | | |
| 1 | BK 7 | 1.5188 | 7.083 | 57.433 | |
| 2 | AIR | 1.00 | 13.303 | 227.443 | |
| 3 | BK 7 | 1.5188 | 5.000 | -44.272 | -3.341 |
| 4 | AIR | 1.00 | | 63.886 | |
| Group 3 | | | | | |
| 1 | BaF 8 | 1.6269 | 21.330 | -768.038 | |
| 2 | AIR | 1.00 | 1.000 | -116.258 | |
| 3 | LaSF N3 | 1.8127 | 14.000 | 326.690 | |
| 4 | AIR | 1.00 | 1.000 | -100.030 | |
| 5 | SF 1 | 1.7231 | 19.998 | 83.182 | -8.604 |
| 6 | AIR | 1.00 | | -15028.439 | |

Table 4 gives the separation and tilt parameters between the relay lens groups and between the relay lens and the CRT faceplate. The location of the vertex of the first surface of group 2 with respect to group 1 is found as follows. Proceed 1 mm along the axis of group 1 as it leaves the vertex of surface 4; move 5.568 mm perpendicular to the axis in an upward direction. Then rotate 8.827° to establish the direction of the axis of group 2, where a positive rotation corresponds to rotating the axis clockwise in Figure 16.

c. SYSTEM CONFIGURATION

Figure 17 shows the system configuration. The parameters that locate the combiner, fold mirror, and first surface of the relay lens are given in Table 5, in which the separation distance is the distance between the element centers and the separation angle is the angle between the surface normal and the line connecting the element centers. For example, the distance between the center of the exit pupil and combiner is 625 mm, measured along a line that makes an angle of 6° to the normal that passes through the center of the exit pupil. The exit pupil is assumed to be vertical with respect to the aircraft cockpit. The sign convention for the tilts in Table 5 is the same as for the group tilts in Table 4. The fold mirror is convex with a radius of curvature of 749.38 mm, and we assumed a BK 7 faceplate for the CRT with a thickness of 3.2 mm.

Figure 18 shows horizontal and vertical ray traces through the system, and indicates how the system fits within the aircraft cockpit. In Figure 18a, the line labelled "CLEARANCE LINE" is a line 0.75 in. inside the inner surface of the F-16 canopy, which is shown without a label. Although the uppermost ray in Figure 18a crosses the clearance line, that ray is outside the ray envelope required by the field-of-view specifications and is shown for completeness in the ray trace.

TABLE 4
RELATIVE LOCATION OF RELAY LENS GROUPS

| | Axial Separation (mm) | Decentration (mm) | Tilt (deg) |
|---|---|---|---|
| Group 1-2 | 1.000 | 5.568 | 8.827 |
| Group 2-3 | 11.103 | 0.200 | 14.719 |
| Group 3-CRT | 52.024 | 0.000 | -34.498 |

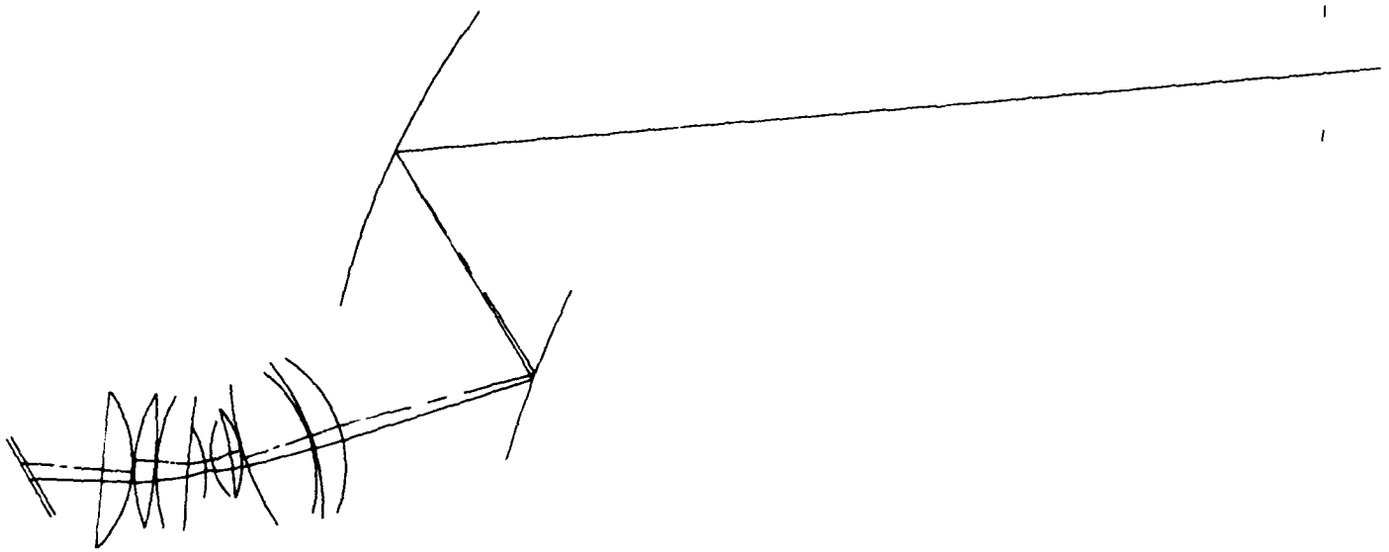

Figure 17. *Optical System Configuration.* The broken line connects the centers or vertices of the elements and the solid line represents a ray at the center of the field-of-view.

TABLE 5
RELATIVE LOCATION OF SYSTEM COMPONENTS

| | Separation Distance (mm) | Separation Angle (deg) | Tilt (deg) |
|---|---|---|---|
| Exit Pupil-to-Combiner | 625.00 | 6.00 | 24.00 |
| Combiner-to-Fold Mirror | 117.07 | 32.65 | -4.37 |
| Fold Mirror-to-Relay Lens | 136.55 | 35.59 | -39.37 |

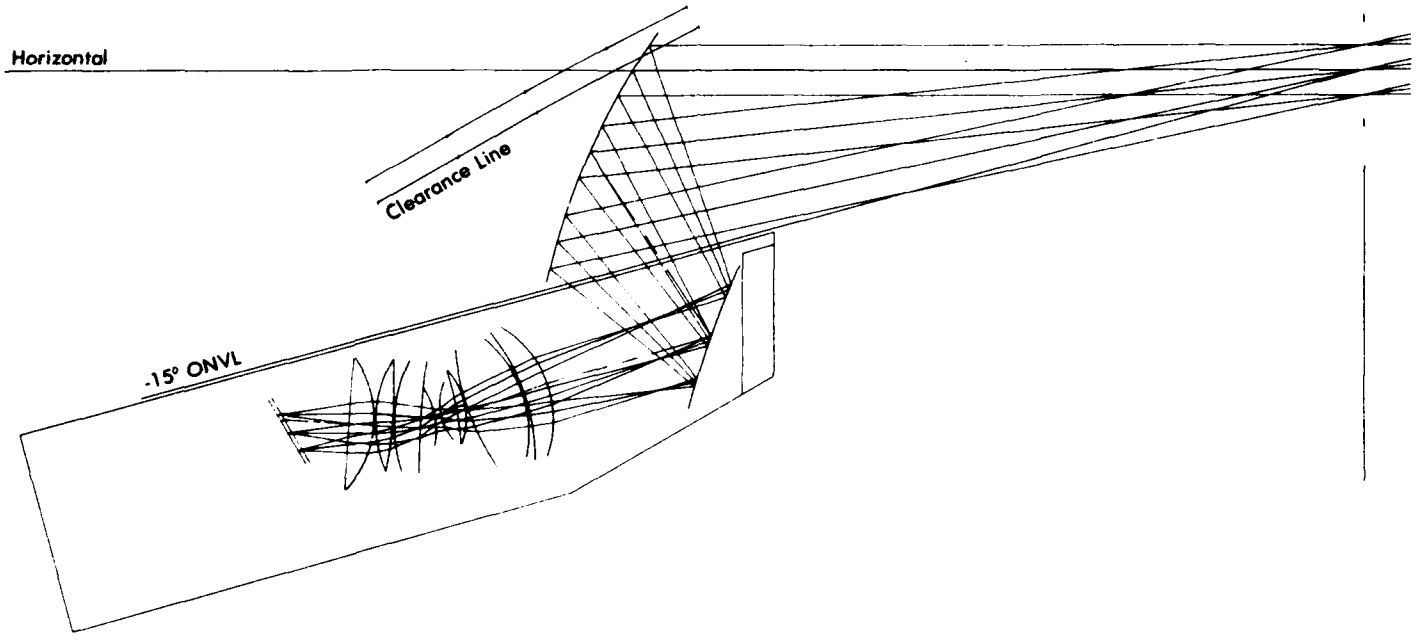


(a) Vertical Ray Trace. The Three Ray Bundles are at Vertical Field Angles of 0, -6, and -12°

Figure 18. Ray Traces through the Optical System

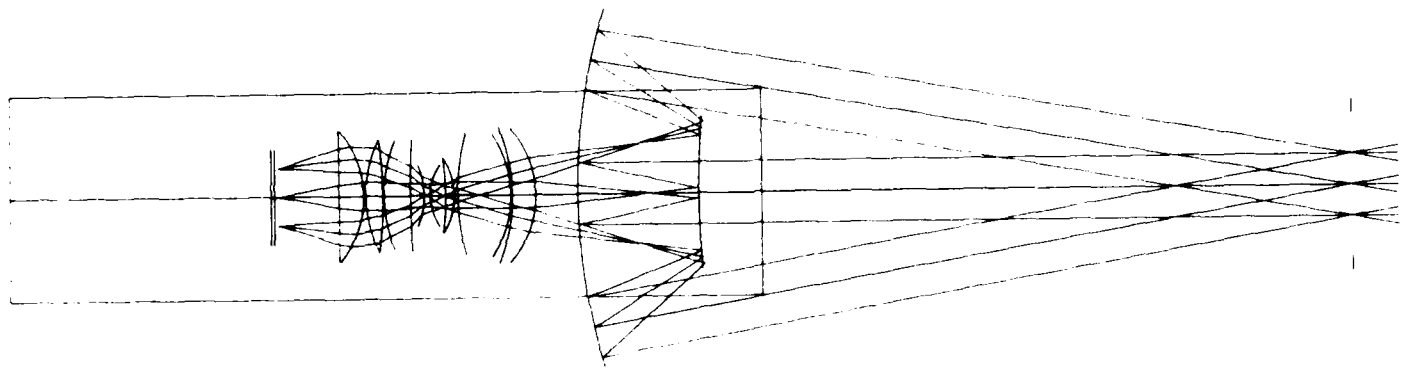

(b) Horizontal Ray Trace. The Three Ray Bundles are at Horizontal Field Angles of -10, 0, and 10°, and at a Vertical Field Angle of -6°

Figure 18. Ray Traces through the Optical System

## SECTION V
## SYSTEM PERFORMANCE

The system was characterized primarily in terms of distortion, ray errors, and hologram efficiency. The system met the goal of less than 0.5 percent distortion over most of the instantaneous field-of-view, and the hologram efficiency was also satisfactory over most of the field. The ray errors exceeded the design goals over much of the field-of-view and exit pupil, but were generally not excessive.

### 1. DISTORTION

Distortion was measured quantitatively by tracing rays from the center of the exit pupil at different field angles and finding their intercepts at the CRT image plane. Figure 19 shows plots of distortion as a function of field angle over the instantaneous vertical and horizontal field-of-view. For these plots, the distortion was measured as follows. A measurement was made very close to the center of the field to determine $\Delta S/\Delta\theta$, the variation $\Delta S$ in image intercept with a small variation $\Delta\theta$ in field angle, from which we calculated a predicted image intercept $S_p$ (relative to the intercept at the center of the field) as a function of the field angle $\theta$,

$$S_p = \frac{\Delta S}{\Delta\theta}\,\theta$$

We calculated the percent distortion D by comparing the measured S values against the predicted $S_p$ values, as

$$D = \frac{S_p - S}{S_p} \times 100$$

In the horizontal direction, the distortion meets the goal of 0.5 percent over the instantaneous and total fields-of-view of $\pm 10^\circ$, with a peak distortion of 0.46 percent distortion at $\pm 10^\circ$. In the vertical direction, the distortion meets the goal from $-12^\circ$ to nearly $-2^\circ$, increasing to a peak of 2.8 percent at an elevation angle of $0^\circ$.

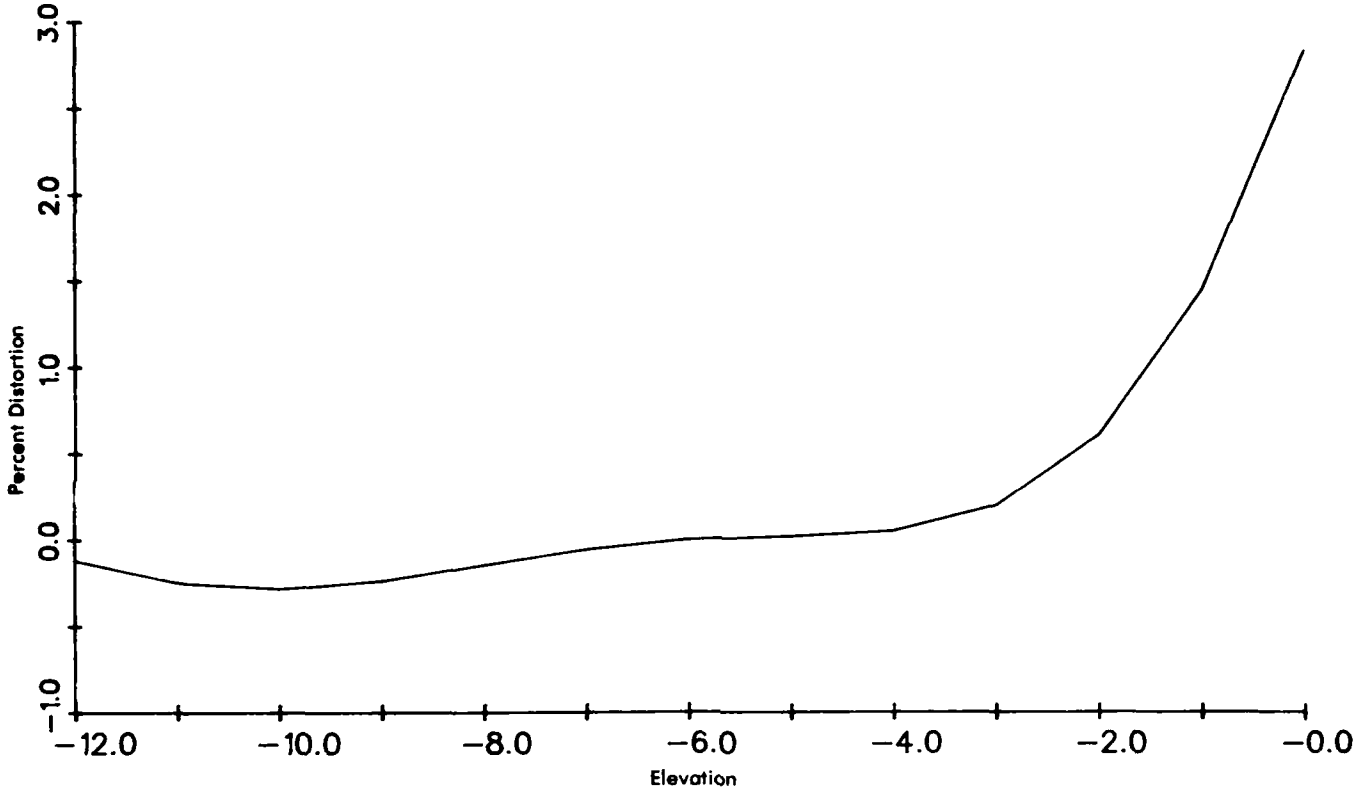


(a) Vertical Field

Figure 19. Distortion Over the Instantaneous Field-of-View

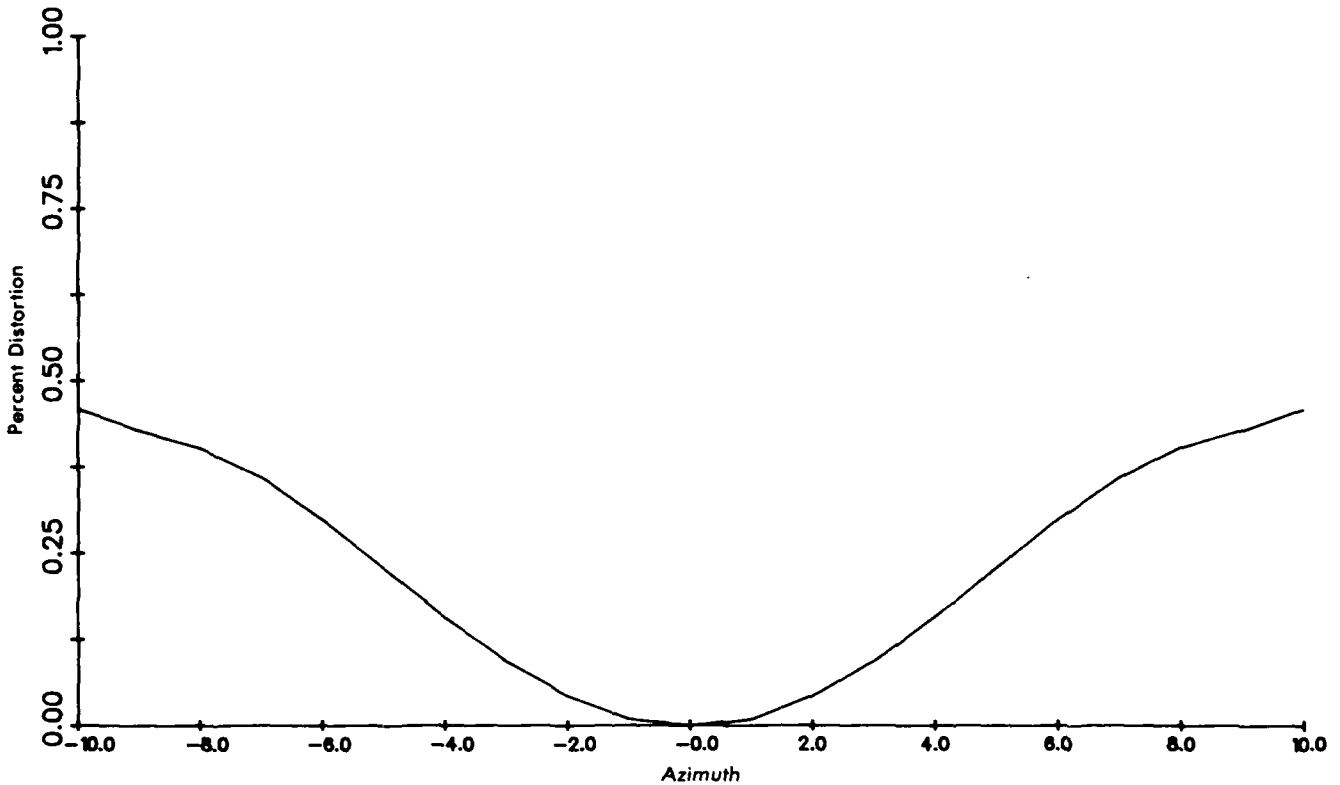


(b) Horizontal Field

Figure 19. Distortion Over the Instantaneous Field-of-View

As the distortion was evaluated over the instantaneous field only during the design optimization, we only show distortion performance over the instantaneous field. This was a result of measuring the distortion from the center of the exit pupil while defining the combiner size such that field angles outside the (vertical) instantaneous field require head motion away from the exit pupil center. Although the hologram could have been extended beyond the intended limits and rays traced from the center of the exit pupil over the total vertical field, such measurements would be of limited meaning. Perhaps a more appropriate solution would have been to define the distortion relative to rays traced from locations in the exit pupil that varied as a function of field angle so that the total field could have been appropriately sampled and measured.

Figure 20 shows the image plane intercepts of a set of rays traced from the center of the exit pupil and distributed over the instantaneous field-of-view in 2° increments. The grid formed by the intercepts has relatively straight lines and regular spacing, although some distortion is still evident, particularly at the corners of the grid.

The distortion performance represents a significant improvement over that of previous holographic HUD systems that we have investigated. Some aspects, however, of the distortion performance of the conventional holographic systems were comparable to the corresponding performance of the aspheric holographic system, but these aspects differed with the individual designs and they represented only a portion of the distortion performance. Figure 21 shows curves of the distortion magnitude as functions of horizontal and vertical field angles for the current system, and for an average of data from conventional holographic HUD systems.

The distortion improvement is particularly evident when plots of image plane intercepts (as in Figure 20) are compared. Figure 22,

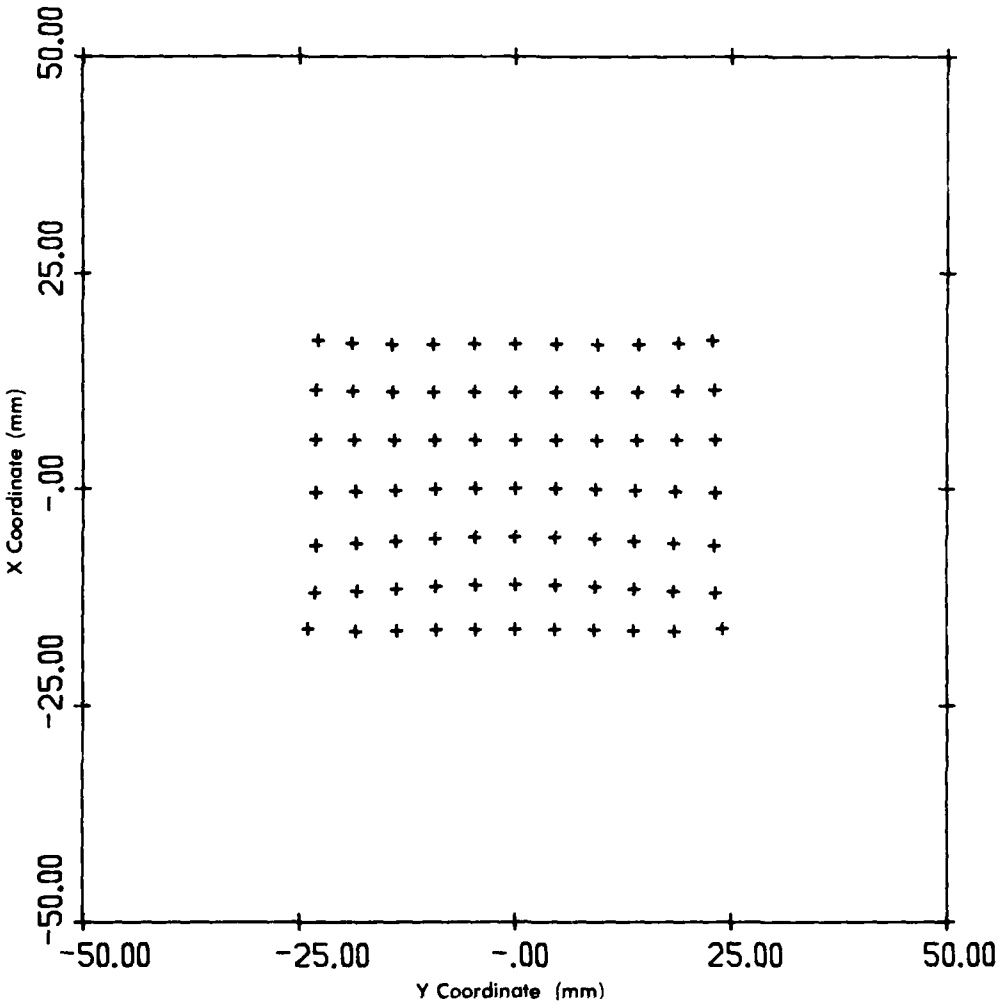


Figure 20. Image Plane Intercepts of a Rayset Distributed Over the Instantaneous Field-of-View in 2° Increments

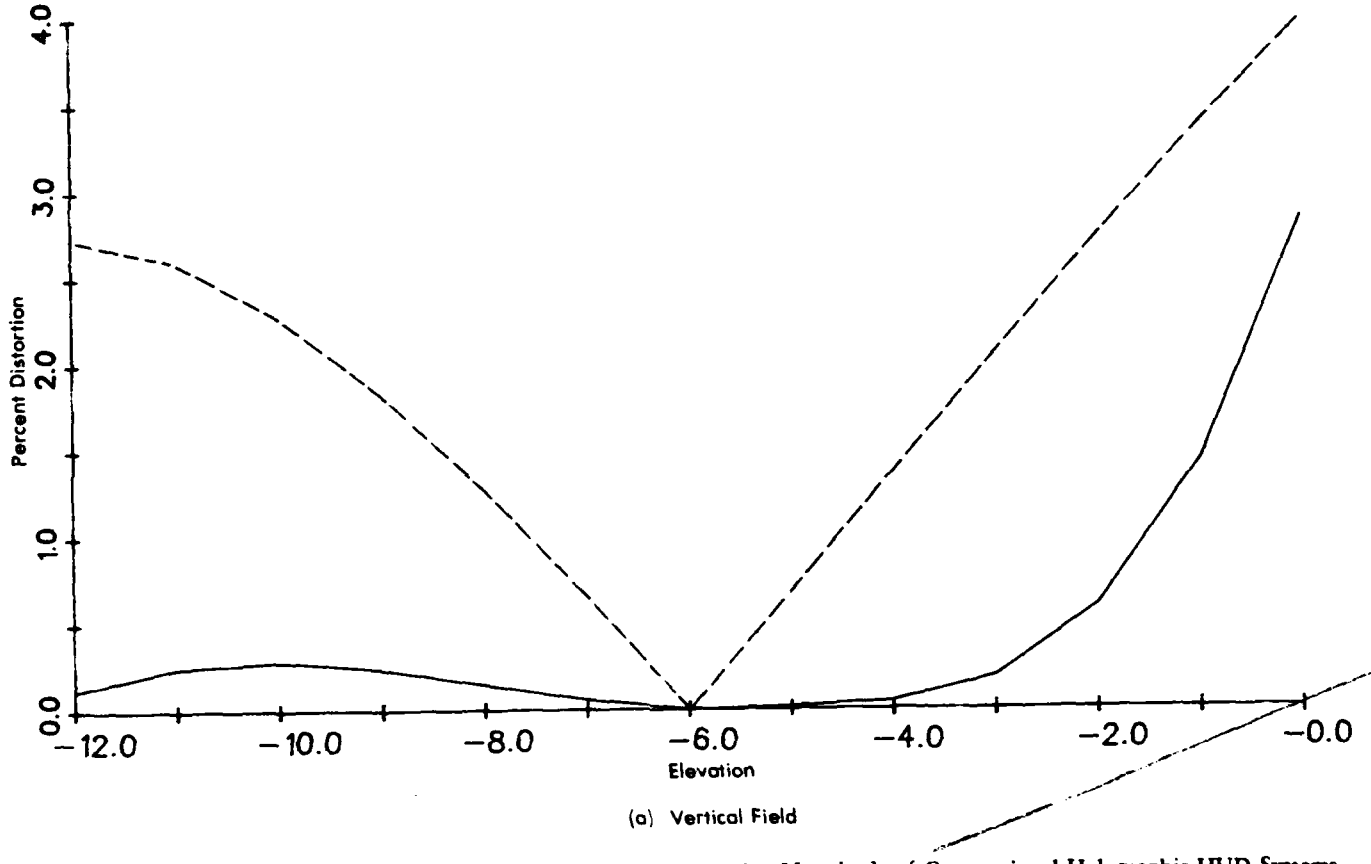


Figure 21. System Distortion Magnitude Compared with Average Distortion Magnitude of Conventional Holographic HUD Systems. Conventional system distortion shown dashed.

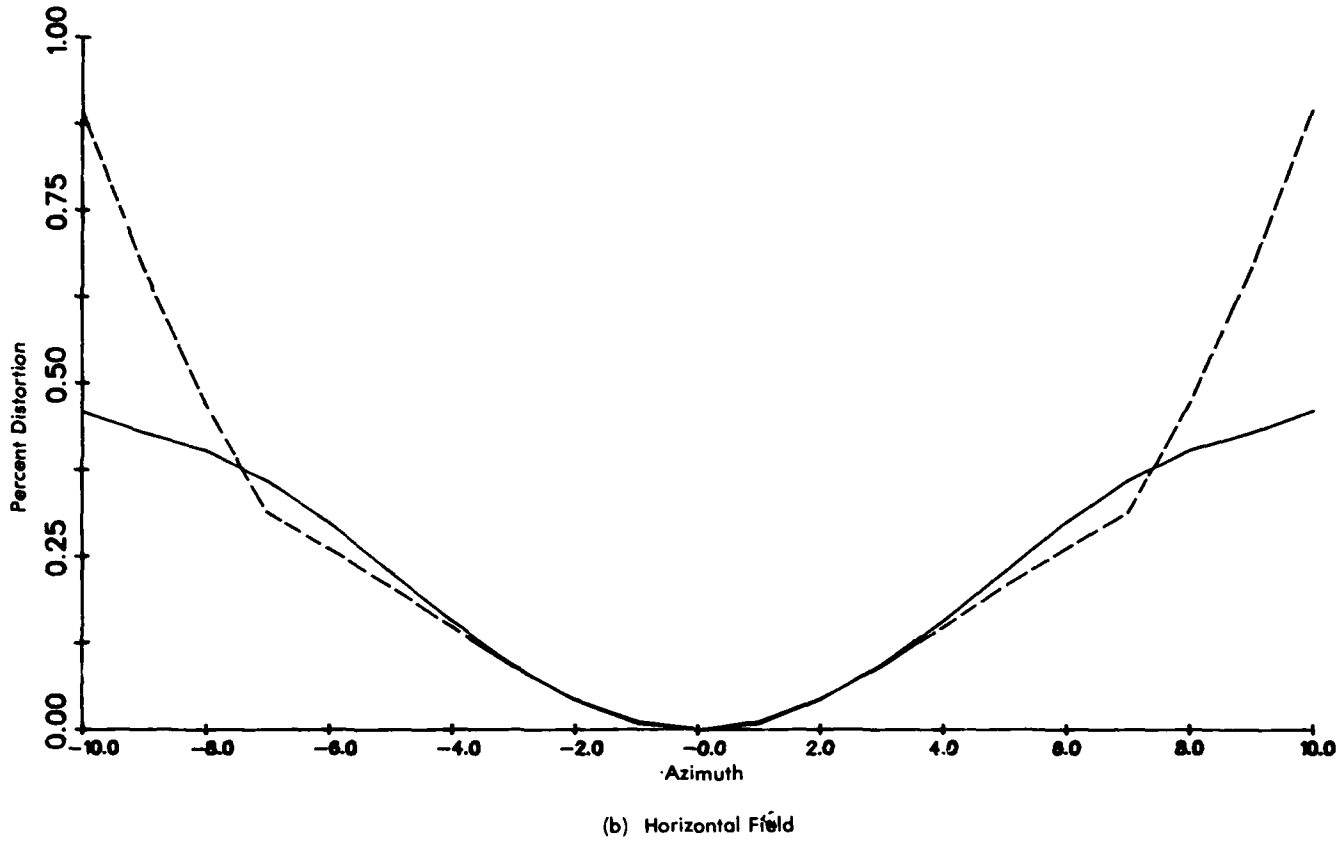


Figure 21. System Distortion Magnitude Compared with Average Distortion Magnitude of Conventional Holographic HUD Systems. Conventional system distortion shown dashed.

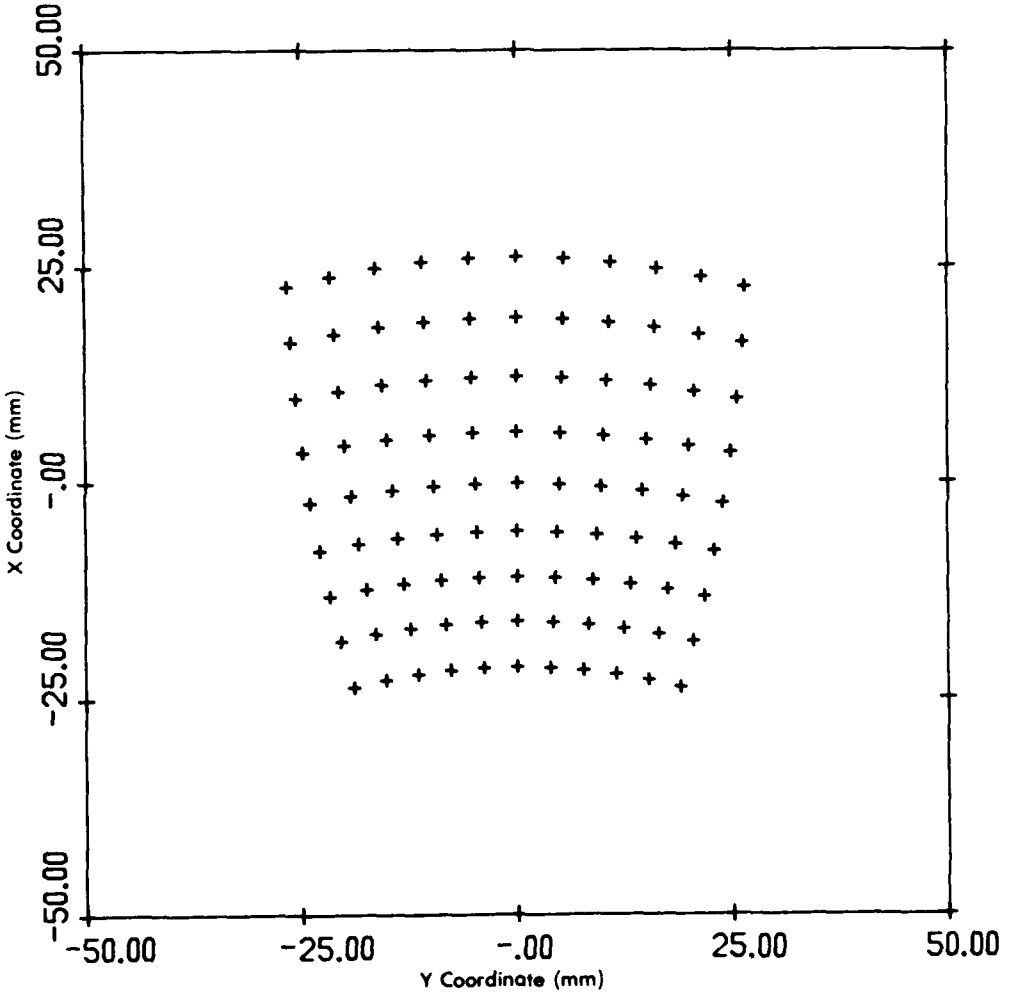


Figure 22. Image Plane Intercepts of a Rayset Uniformly Distributed Over a 12 x 20° Field-of-View for a Conventional Holographic HUD System

for example, shows the image plane intercepts corresponding to a 12 x 20° field for a system in which the preliminary combiner design discussed in Section III.1b was combined with the initial relay lens design. While the system was far from optimum, the distortion shown in Figure 22 is indicative of the distortion typically found in holographic HUD systems.

## 2. RAY ERRORS

We measured ray errors by generating ray intercept curves at the CRT image surface and by measuring the reticle parallax and reticle accuracy at the exit pupil. Ray intercept curves are shown in Figure 23 for angles covering the instantaneous field-of-view. These curves were generated by tracing fans of parallel rays from the exit pupil to the CRT image surface as described previously for the intermediate image surface. In Figure 23, the vertical axes correspond to a displacement of ±1 mm, which, in turn, corresponds to an angular error at the exit pupil of approximately ±6.8 mr. The curves represent elevation angles (denoted by $\alpha$) of 0, -3, -6, -9, and -12°, and azimuth angles (denoted by $\beta$) of 0, -3.3, -6.7, and -10°; because of symmetry, the curves would have the same appearance for positive azimuth angles.

The ray intercept curves are useful as they indicate the types of aberration remaining in the optical system. At the field angles shown, sphrical aberration is the primary residual aberration, with a lesser amount of uncorrected coma present.

Figure 24 shows ray intercept curves made at elevation angles of +3° and -15°, 3° in each direction beyond the limits of the vertical instantaneous field-of-view. For the curves at +3°, the fans were centered 1.0 cm below the center of the eyebox whereas for the curves at -15°, the fans were centered 1.0 cm above the center of the eyebox. Considerable coma and spherical aberration are evident in the

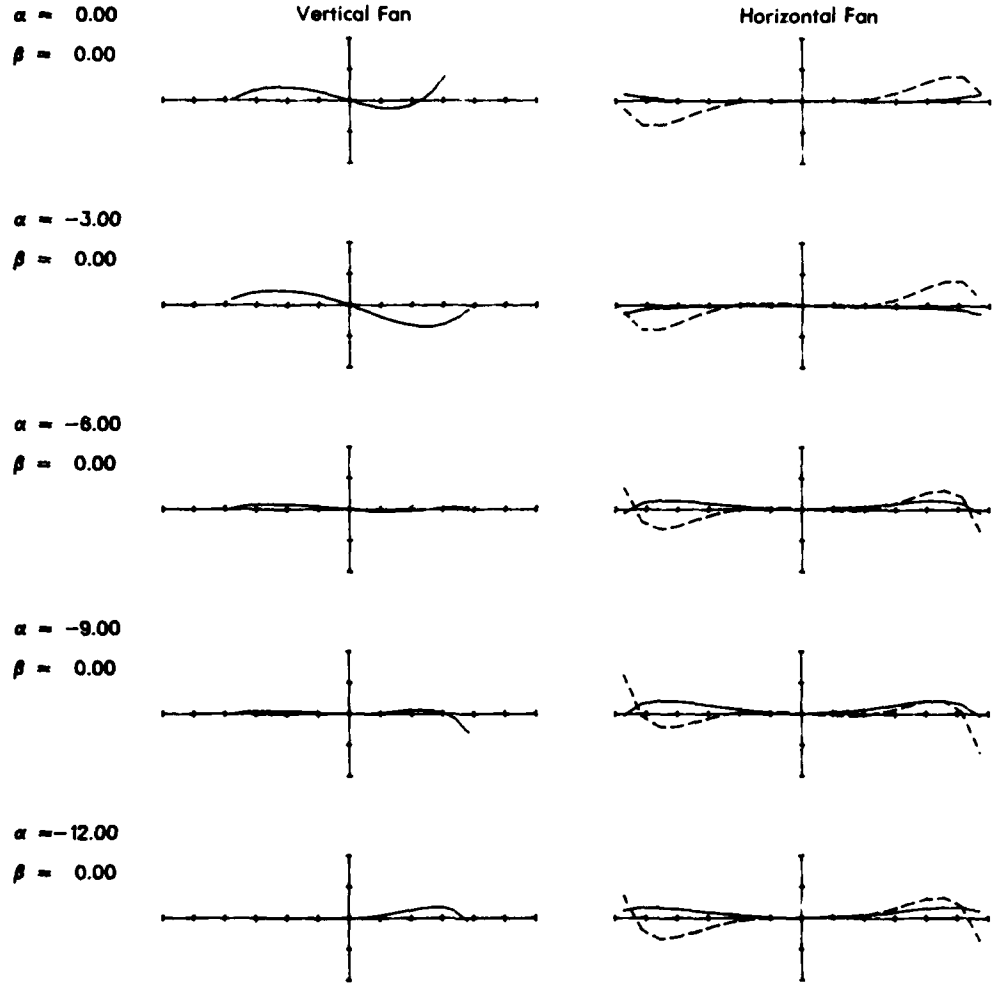


(a) Vertical Field Angles

Figure 23. Ray Intercept Curves for the Optical System at Five Vertical Field Angles and Three Horizontal Field Angles. The distance between tick marks on the horizontal axes is 10 mm; the distance between tick marks on the vertical axes is 0.5 mm.

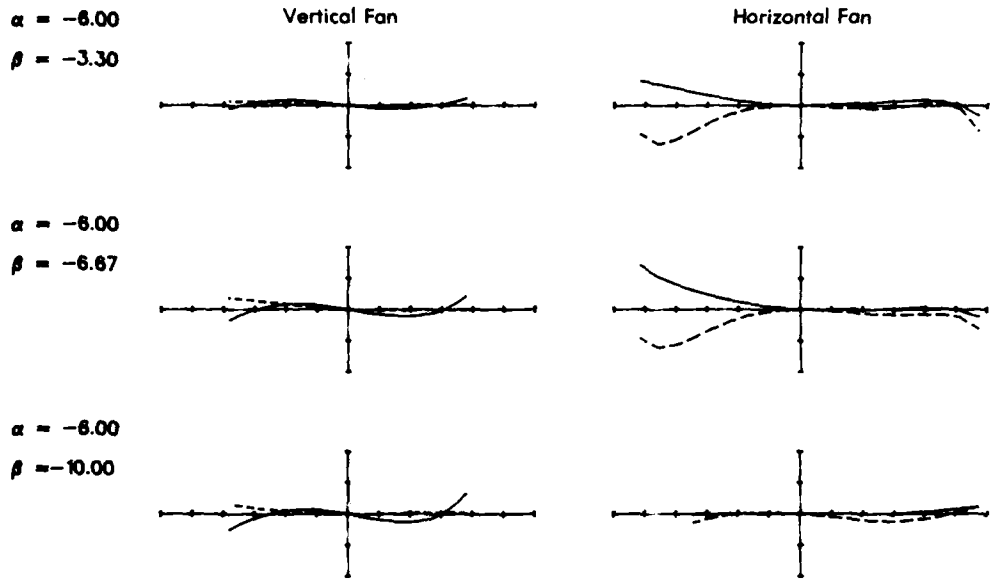


(b) Horizontal Field Angles

Figure 23. Ray Intercept Curves for the Optical System at Five Vertical Field Angles and Three Horizontal Field Angles. The distance between tick marks on the horizontal axes is 10 mm; the distance between tick marks on the vertical axes is 0.5 mm.

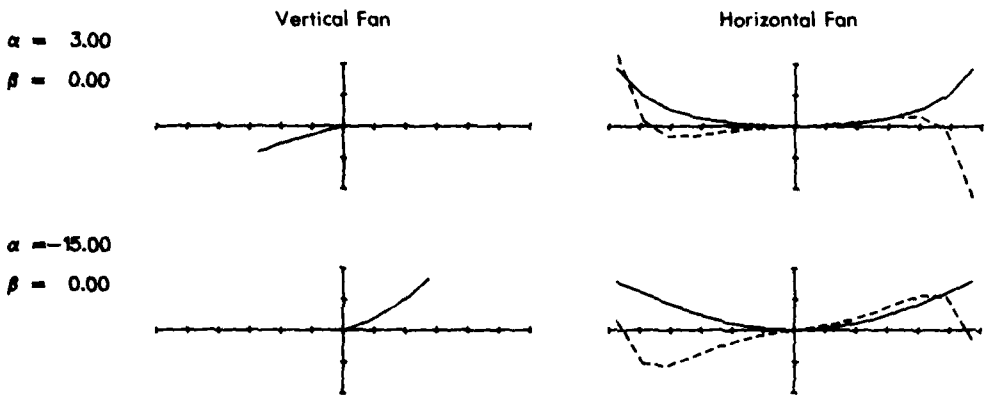


Figure 24. Ray Intercept Curves for the Optical System at Two Vertical Field Angles Beyond the Extent of the Vertical Instantaneous Field-of-View. The distance between tick marks on the horizontal axes is 10 mm; the distance between tick marks on the vertical axes is 0.5 mm.

curves drawn for the horizontal fans, a result of our limiting the rayset used in the system optimization to the instantaneous field.

Although the ray intercept curves provide useful insights into the behavior and performance of the system, the performance criteria of greatest ultimate interest are the accuracy and parallax errors at the exit pupil. As a measure of these errors, we determined the reticle accuracy and the reticle parallax as follows. In each case, the method was based on finding the actual ray angles at the two eye positions that corresponded to some nominal field angle. Assuming a distortion-free system, we determined a CRT location corresponding to a nominal field angle. Then, for a given head location, we found the rays passing through the two eye locations that reached the CRT location corresponding to the nominal field angle. The ray errors were the differences in elevation $\Delta\alpha$ and in azimuth $\Delta\beta$ between the actual ray angles and the nominal field angles. The right eye errors are thus

$$\Delta\alpha_R = \alpha_{right} - \alpha_{nom.}$$

$$\Delta\beta_R = \beta_{right} - \beta_{nom.}$$

and a similar set of equations define $\Delta\alpha_L$ and $\Delta\beta_L$ for the left eye errors.

Reticle accuracy was then calculated as the root-sum-square of the ray errors averaged between the two eyes, which can be expressed as

$$\text{Reticle accuracy} = \left[\left(\frac{\Delta\alpha_R + \Delta\alpha_L}{2}\right)^2 + \left(\frac{\Delta\beta_R + \Delta\beta_L}{2}\right)^2\right]^{1/2} \quad (46)$$

At field angles and head locations where the display was not visible to both eyes, reticle accuracy was computed as the root-sum-square of the errors corresponding to the eye for which the display was visible.

Reticle parallax was calculated as the root-sum-square of the differences in the errors at the two eye locations, or

$$\text{Reticle parallax} = \left[ (\Delta\alpha_R - \Delta\alpha_L)^2 + (\Delta\beta_R - \Delta\beta_L)^2 \right]^{1/2} \qquad (47)$$

Where the display was not visible to both eyes, there could be no parallax and therefore no calculation was made.

We determined the reticle accuracy and reticle parallax as a function of head position at each of a number of field angles. The size of the exit pupil, 3.0 in. vertical by 4.5 in. horizontal permitted head motion of ±1.5 in. vertical by ±1.0 in. horizontal, keeping both eyes within the exit pupil. Figure 25 shows curves of reticle accuracy and reticle parallax as functions of horizontal head position (in inches) at the center of the field. The three curves in each plot represent different vertical head positions, with the solid line for the head centered, the short dashes for the head raised by 1.0 inch, and the long dashes for the head lowered by 1.0 inch. The data were taken at horizontal intervals of 0.2 inch. The accuracy data average to 0.88 mr with a peak of 2.1 mr occurring for the head raised position. The parallax errors are somewhat more severe, with a 2.0 mr average and a peak of 3.8 mr, again for the head raised position. We found that over most of the field-of-view, the parallax errors were comparable to, or more severe than, the accuracy errors.

Similar plots of reticle accuracy and reticle parallax for other field angles are shown in Figures 26-28, where the data in Figures 26, 27, and 28 represent angular displacements of 2.5, 5.0, and 7.5°, respectively, from the center of the field-of-view. The errors are greatest at the edges of the exit pupil and for elevation angles corresponding to upward looks. The large errors at upward looks are in part a result of the greater distortion at those field angles, as we compute the errors assuming a distortion-free system. Table 6

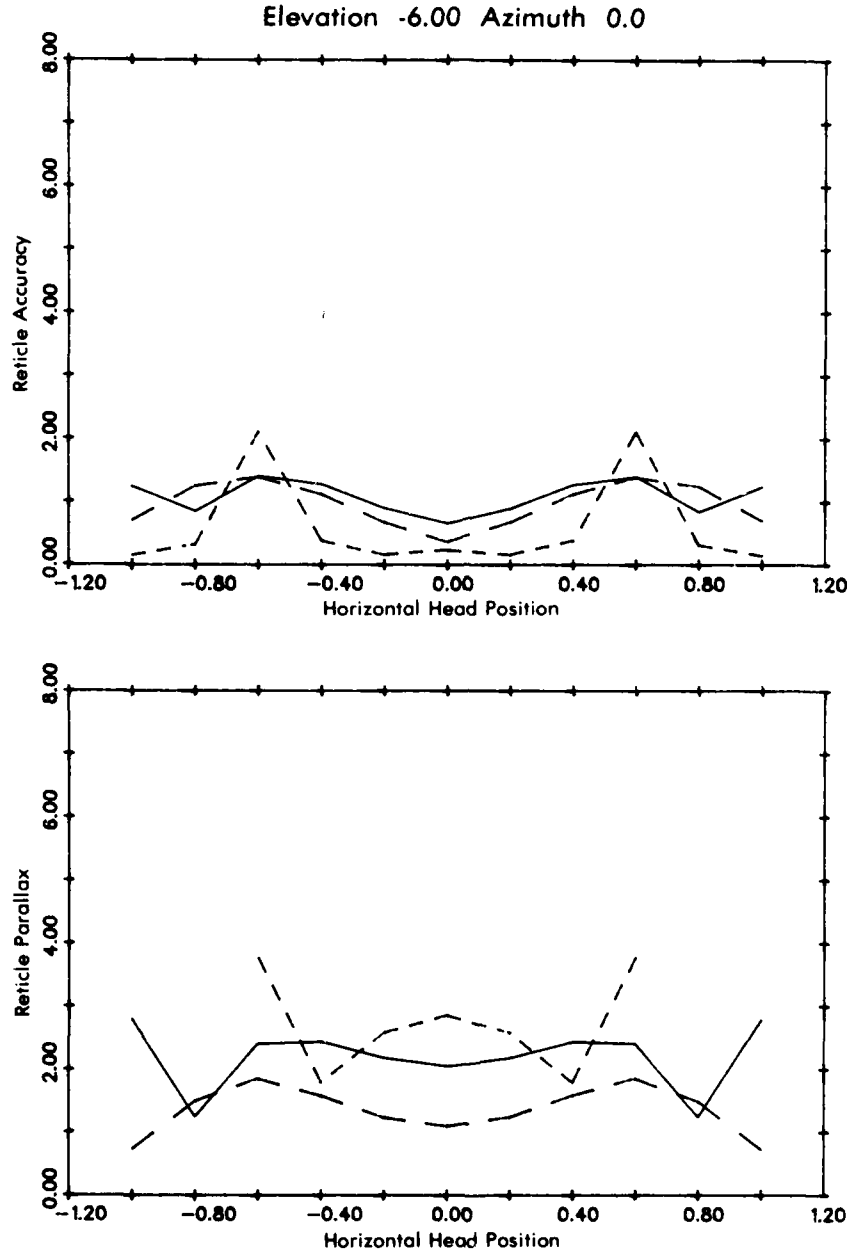


Figure 25. Reticle Accuracy and Reticle Parallax As Functions of Head Position for the Center of the Field-of-View. The solid line corresponds to the head centered vertically, the short dashes to the head raised 1.0 inch, and the long dashes to the head lowered 1.0 inch.

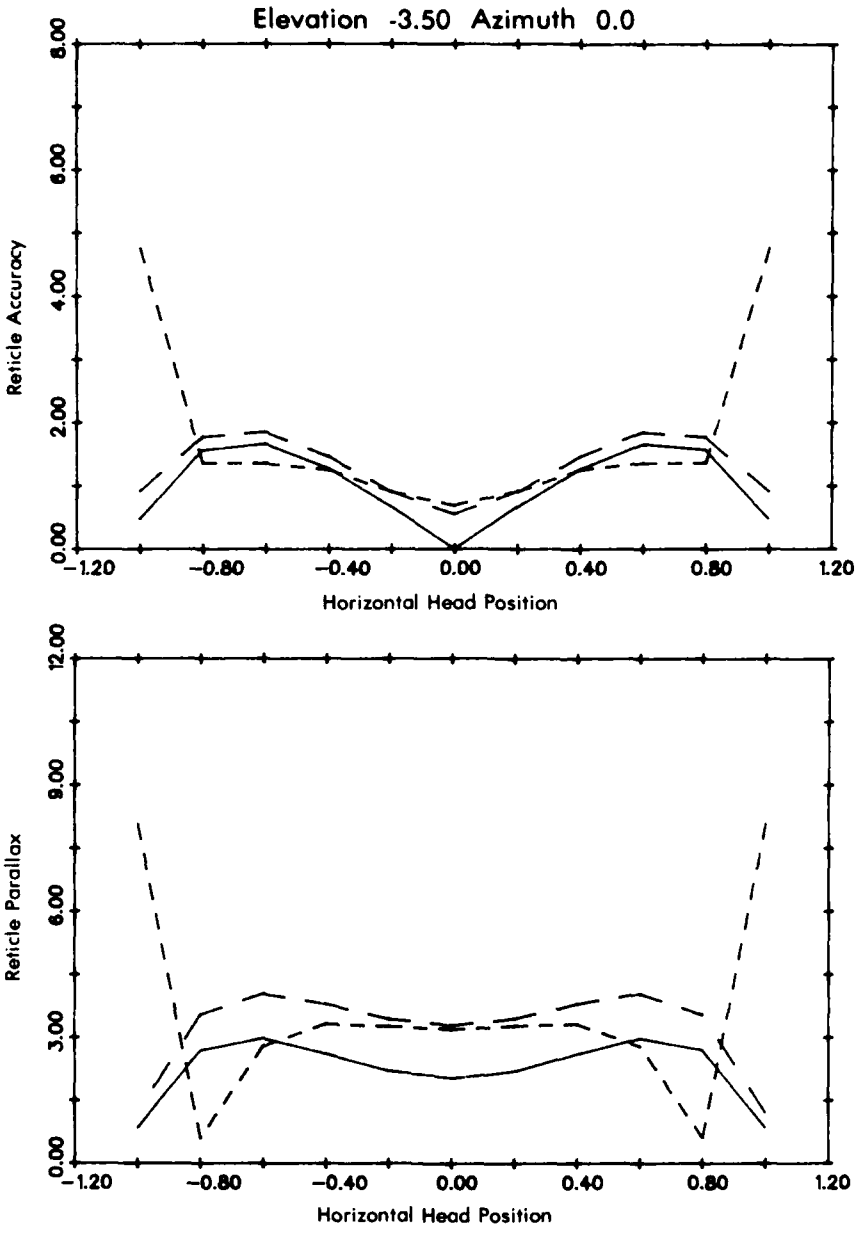


(a) 2.5° Upward Displacement

Figure 26. Reticle Accuracy and Reticle Parallax As Fucntions of Head Position for Field Angles Displaced by 2.5° from the Center of the Field. The solid line corresponds to the head centered vertically, the short dashes to the head raised 1.0 inch, and the long dashes for the head lowered 1.0 inch.

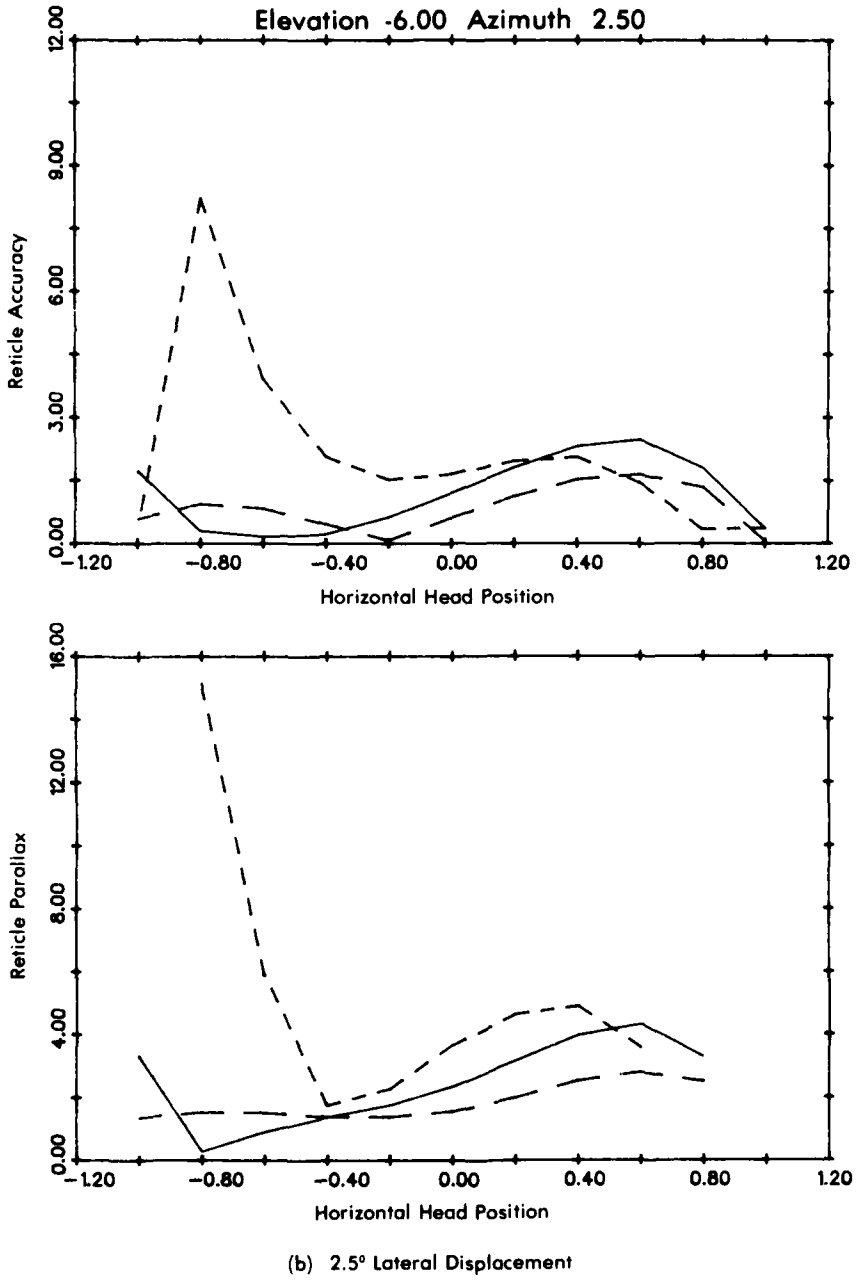


(b) 2.5° Lateral Displacement

Figure 26. Reticle Accuracy and Reticle Parallax As Functions of Head Position for Field Angles Displaced by 2.5° from the Center of the Field. The solid line corresponds to the head centered vertically, the short dashes to the head raised 1.0 inch, and the long dashes for the head lowered 1.0 inch.

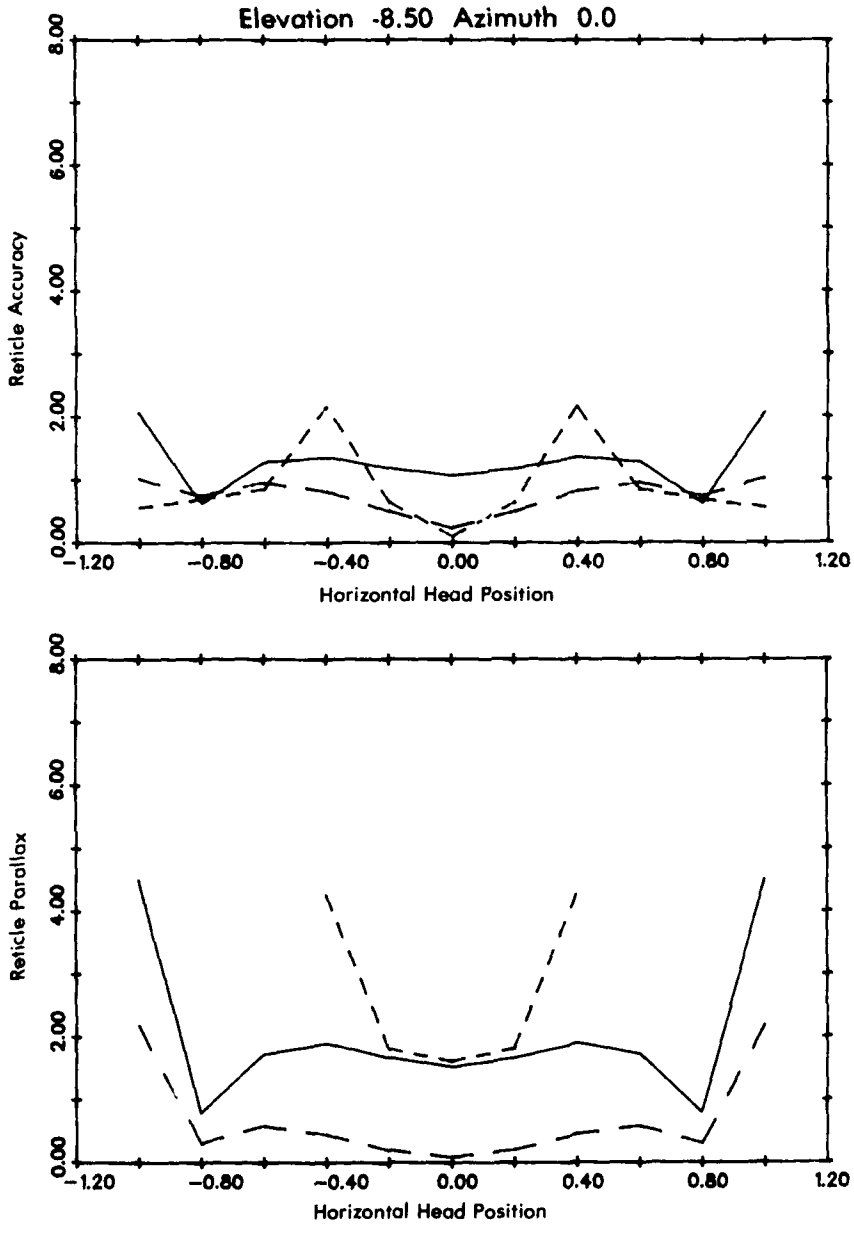


(c) 2.5° Downward Displacement

Figure 26. Reticle Accuracy and Reticle Parallax As Functions of Head Position for Field Angles Displaced by 2.5° from the Center of the Field. The solid line corresponds to the head centered vertically, the short dashes to the head raised 1.0 inch, and the long dashes for the head lowered 1.0 inch.

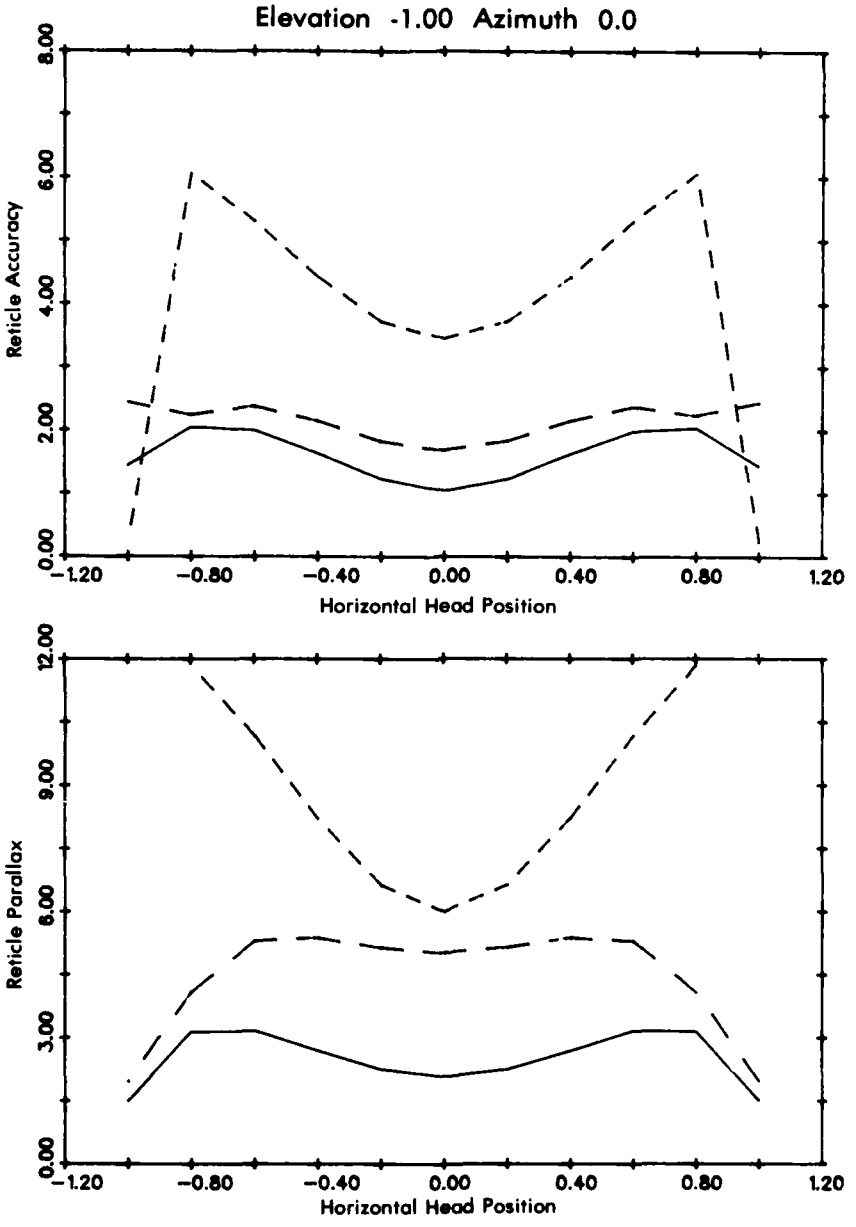


(a) 5.0° Upward Displacement

Figure 27. Reticle Accuracy and Reticle Parallax As Functions of Head Position for Field Angles Displaced by 5.0° from the Center of the Field. The solid line corresponds to the head centered vertically, the short dashes to the head raised 1.0 inch, and the long dashes for the head lowered 1.0 inch.

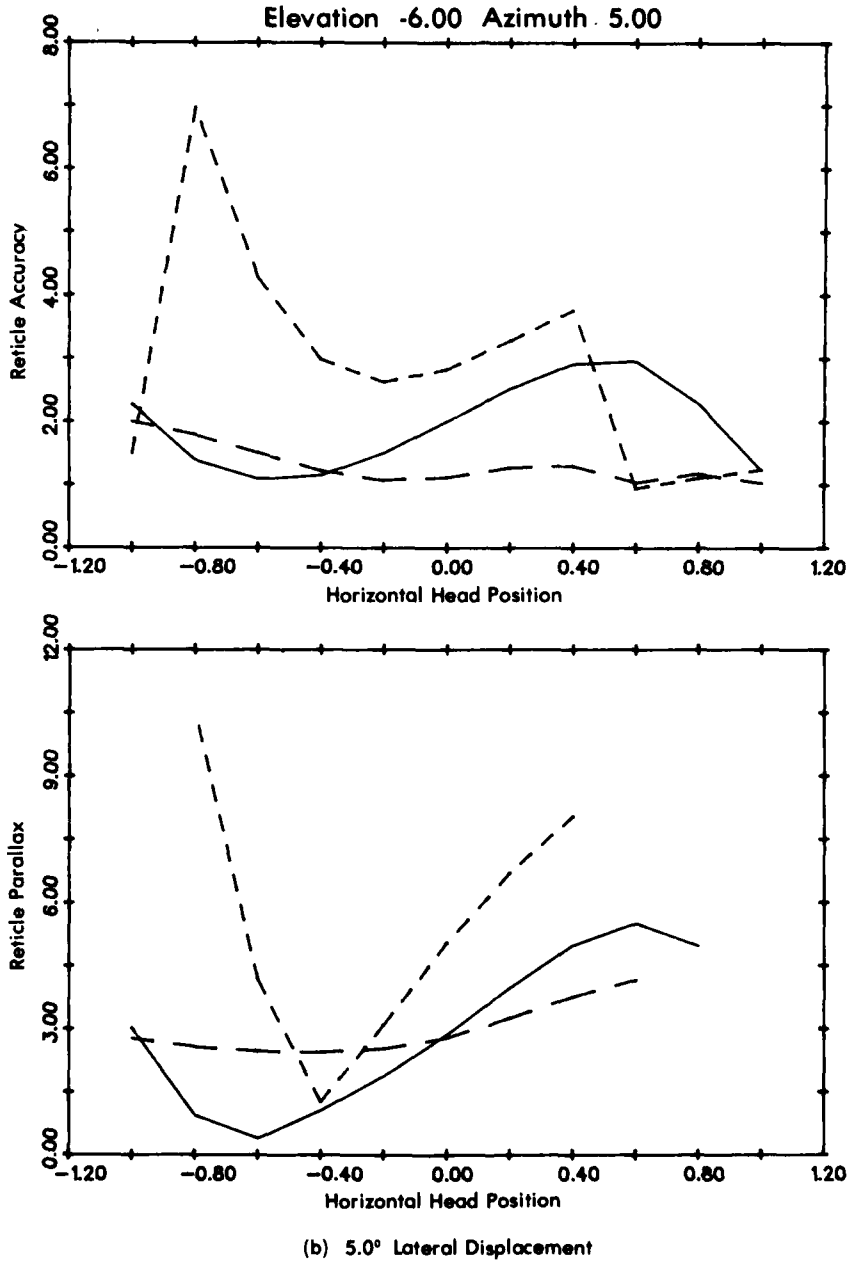


(b) 5.0° Lateral Displacement

Figure 27. Reticle Accuracy and Reticle Parallax As Functions of Head Position for Field Angles Displaced by 5.0° from the Center of the Field. The solid line corresponds to the head centered vertically, the short dashes to the head raised 1.0 inch, and the long dashes for the head lowered 1.0 inch.

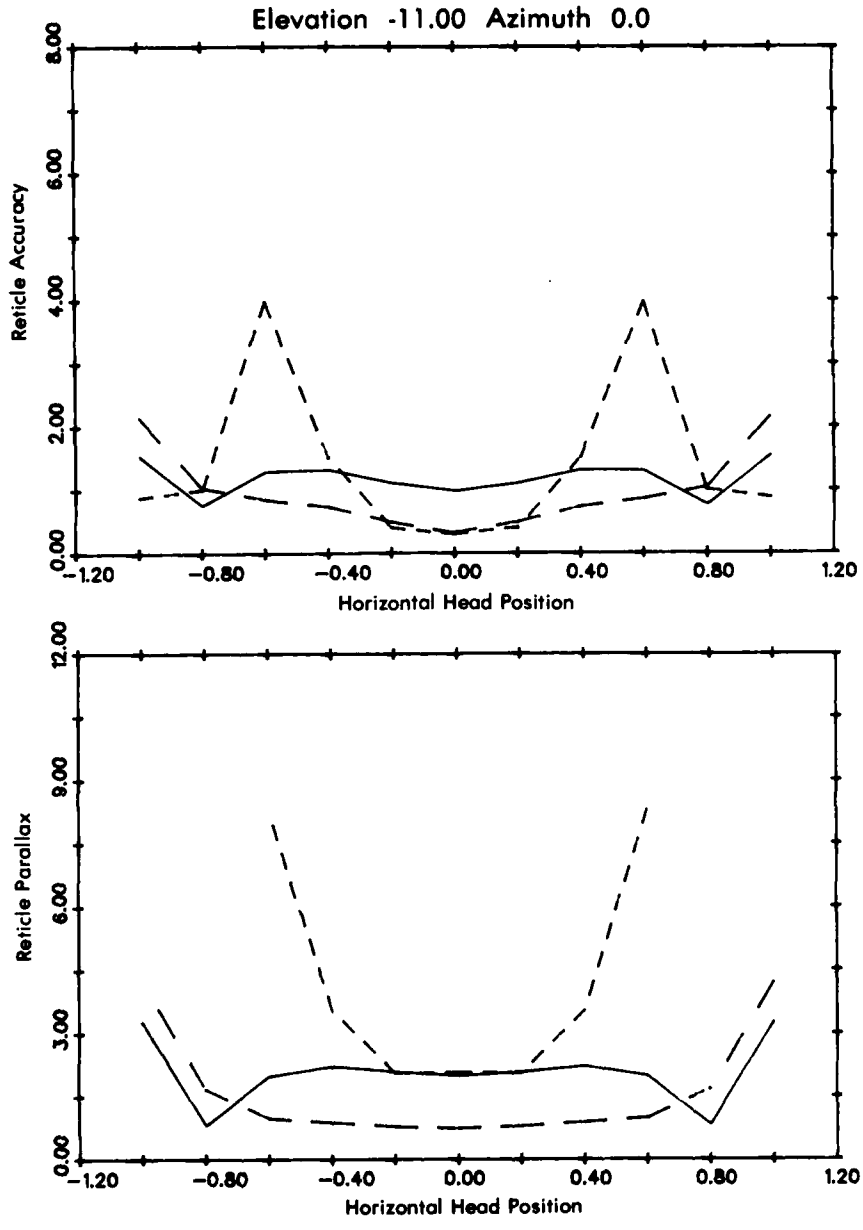


(c) 5.0° Downward Displacement

Figure 27. Reticle Accuracy and Reticle Parallax As Functions of Head Position for Field Angles Displaced by 5.0° from the Center of the Field. The solid line corresponds to the head centered vertically, the short dashes to the head raised 1.0 inch, and the long dashes for the head lowered 1.0 inch

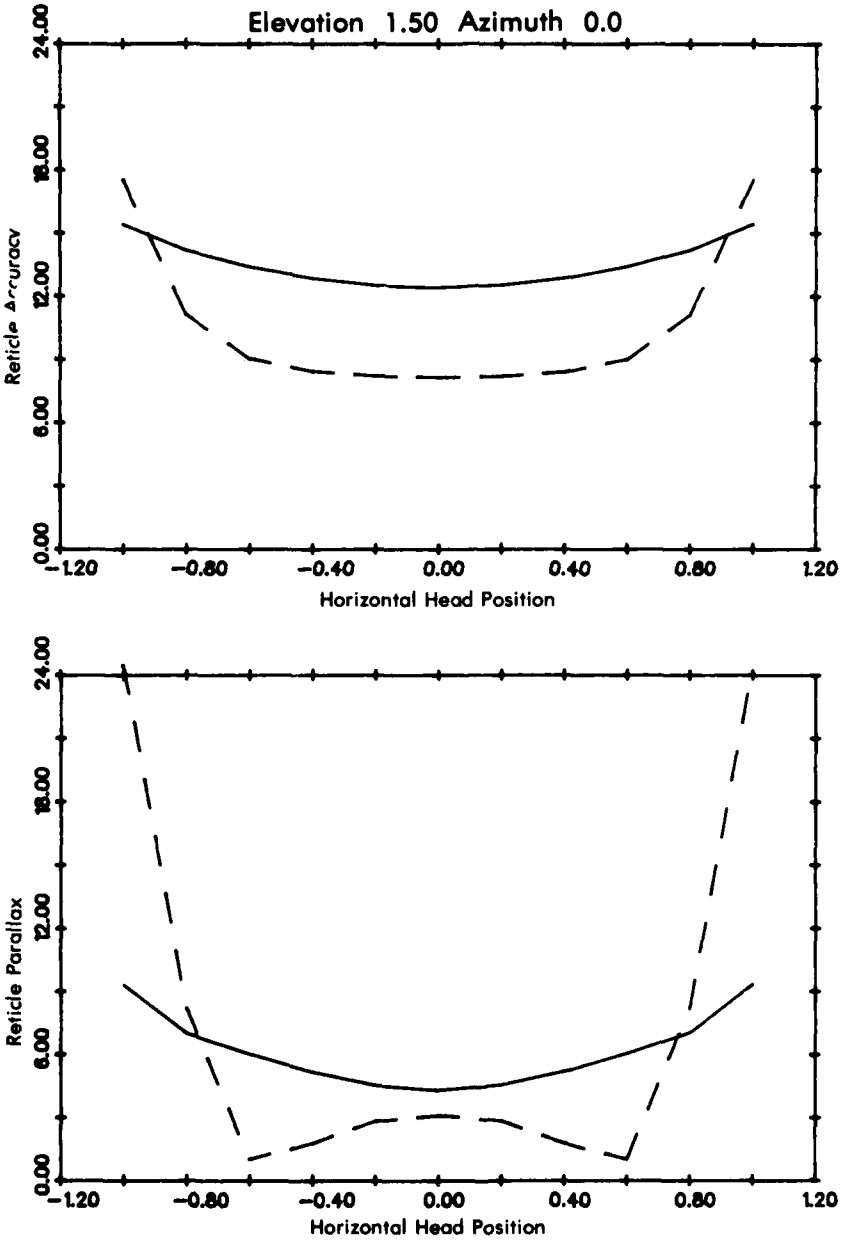


(a) 7.5° Upward Displacement

Figure 28. Reticle Accuracy and Reticle Parallax As Functions of Head Position for Field Angles Displaced by 7.5° from the Center of the Field. The solid line corresponds to the head centered vertically, and the long dashes for the head lowered 1.0 inch.

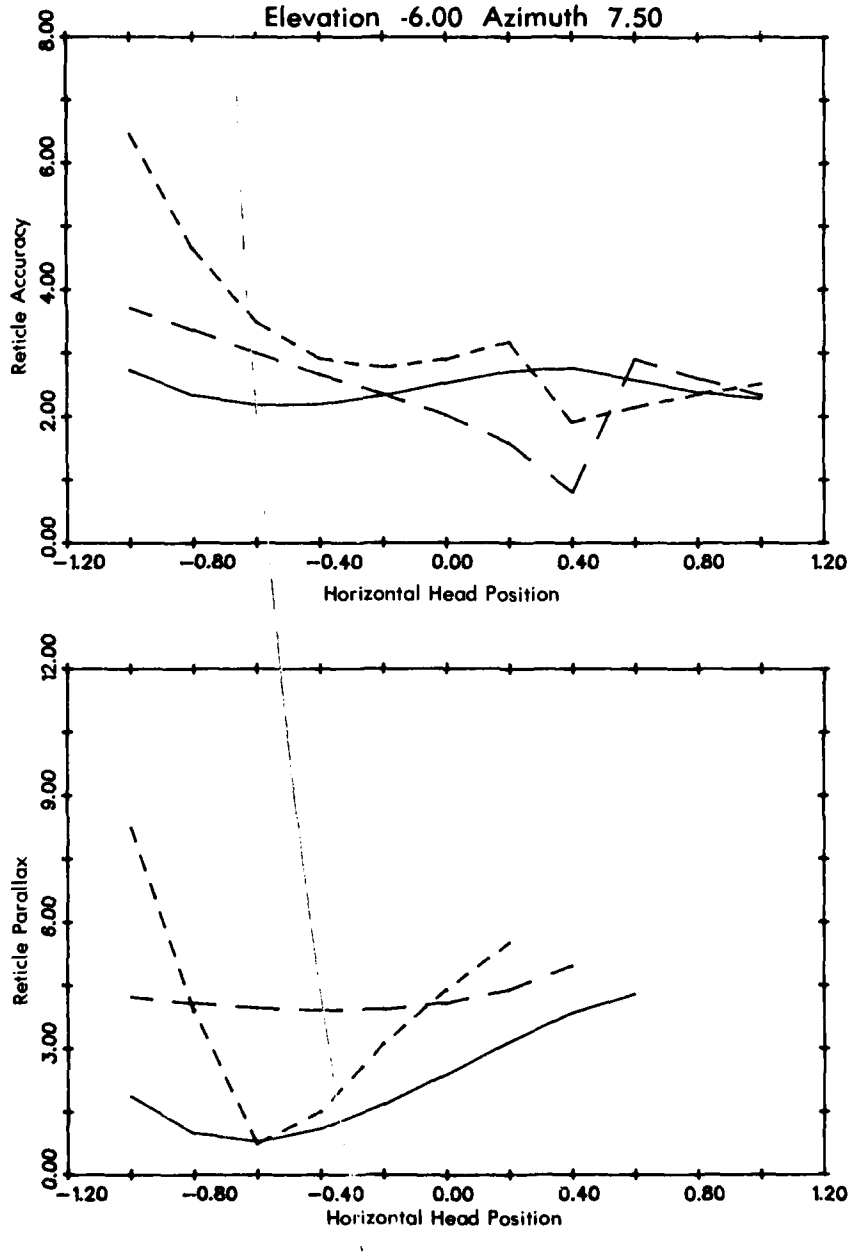


(b) 7.5° Lateral Displacement

Figure 28. Reticle Accuracy and Reticle Parallax As Functions of Head Postion for Field Angles Displaced by 7.5° from the Center of the Field. The solid line corresponds to the head centered vertically, the short dashes to the head raised 1.0 inch, and the long dashes for the head lowered 1.0 inch.

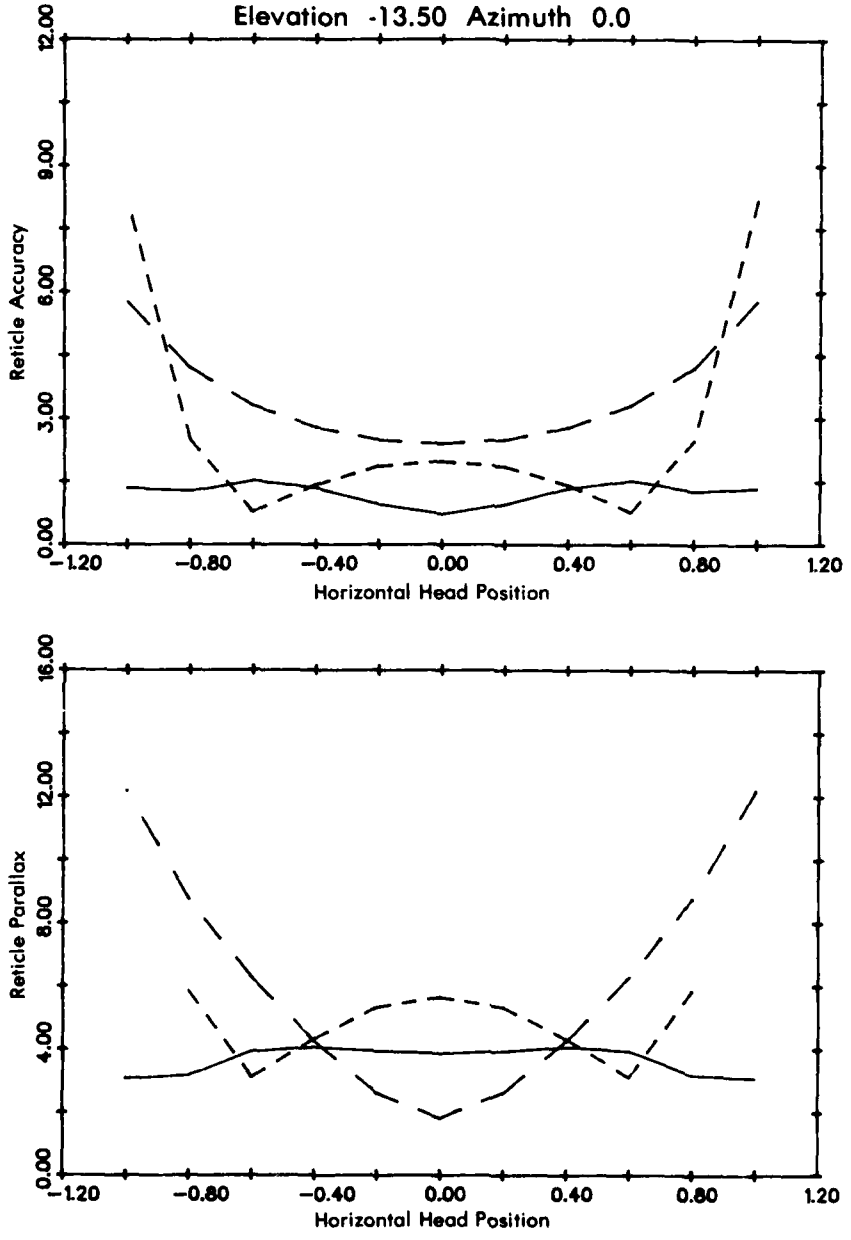


(c) 7.5° Downward Displacement

Figure 28. Reticle Accuracy and Reticle Parallax As Functions of Head Position for Field Angles Displaced by 7.5° from the Center of the Field. The solid line corresponds to the head centered vertically, the short dashes to the head raised 1.0 inch, and the long dashes for the head lowered 1.0 inch.

TABLE 6
RETICLE PARALLAX AND ACCURACY ERRORS

| | | Parallax | | | Accuracy | | |
|---|---|---|---|---|---|---|---|
| α | β | Goal | Average | Maximum | Goal | Average | Maximum |
| -6.0 | 0.0 | 0.6 | 2.01 | 3.77 | 0.8 | 0.88 | 2.10 |
| -3.5 | 0.0 | 0.6 | 3.01 | 8.08 | 1.0 | 1.39 | 4.77 |
| -6.0 | 2.5 | 0.6 | 3.04 | 15.14 | 1.0 | 1.40 | 8.22 |
| -8.5 | 0.0 | 0.6 | 1.63 | 4.51 | 1.0 | 0.98 | 2.15 |
| -1.0 | 0.0 | 2.0 | 5.04 | 11.84 | 2.0 | 2.56 | 6.06 |
| -6.0 | 5.0 | 2.0 | 3.66 | 10.55 | 2.0 | 2.04 | 6.96 |
| -11.0 | 0.0 | 2.0 | 2.43 | 8.29 | 2.0 | 1.20 | 3.97 |
| 1.5 | 0.0 | 2.0 | 7.90 | 33.39 | 3.0 | 16.51 | 35.25 |
| -6.0 | 7.5 | 2.0 | 3.38 | 8.26 | 3.0 | 2.72 | 6.47 |
| -13.5 | 0.0 | 2.0 | 4.94 | 12.19 | 3.0 | 2.56 | 8.17 |

All angles in degrees and errors in milliradians

contains for each field angle the maximum and average error of the data shown in Figures 25-28, and the parallax and accuracy design goals. As in the ray intercept plots, the elevation angles are denoted by $\alpha$ and the azimuth angles by $\beta$.

## 3. EFFICIENCY

A major factor affecting the brightness uniformity of the system is the hologram diffraction efficiency. We computed the diffraction efficiency of rays distributed over the vertical field and over the vertical extent of the exit pupil. All rays used to evaluate the hologram efficiency were in the vertical plane bisecting the optical system (the xz-plane in our coordinate frame), as the analysis we use assumes that the plane of incidence is parallel to the hologram grating vector.

Figure 29 shows curves of diffraction efficiency as a function of vertical field angle for head positions corresponding to the top, center, and bottom of the exit pupil. We assumed a volume phase hologram with a thickness of 10 $\mu$m and a refractive index modulation of 0.04. The rays sampled the system at 1° increments, with some rays vignetted by the optical system. From the center and bottom of the exit pupil, the efficiency exceeded 90 percent for all rays. From the top of the exit pupil, the uniformity is much less, with rays at the upper field angles strongly attenuated by the hologram. If we assume that 75 percent of the vertical instantaneous field-of-view should be visible from the upper edge of the exit pupil, then the required field coverage extends from an elevation angle of -16° to -8°; over this field, the efficiency is everywhere above 60 percent.

The design procedure was intended to produce a symmetric uniformity, such that if the efficiency from the top of the exit pupil decreased at the upper elevation angles, then the efficiency from the

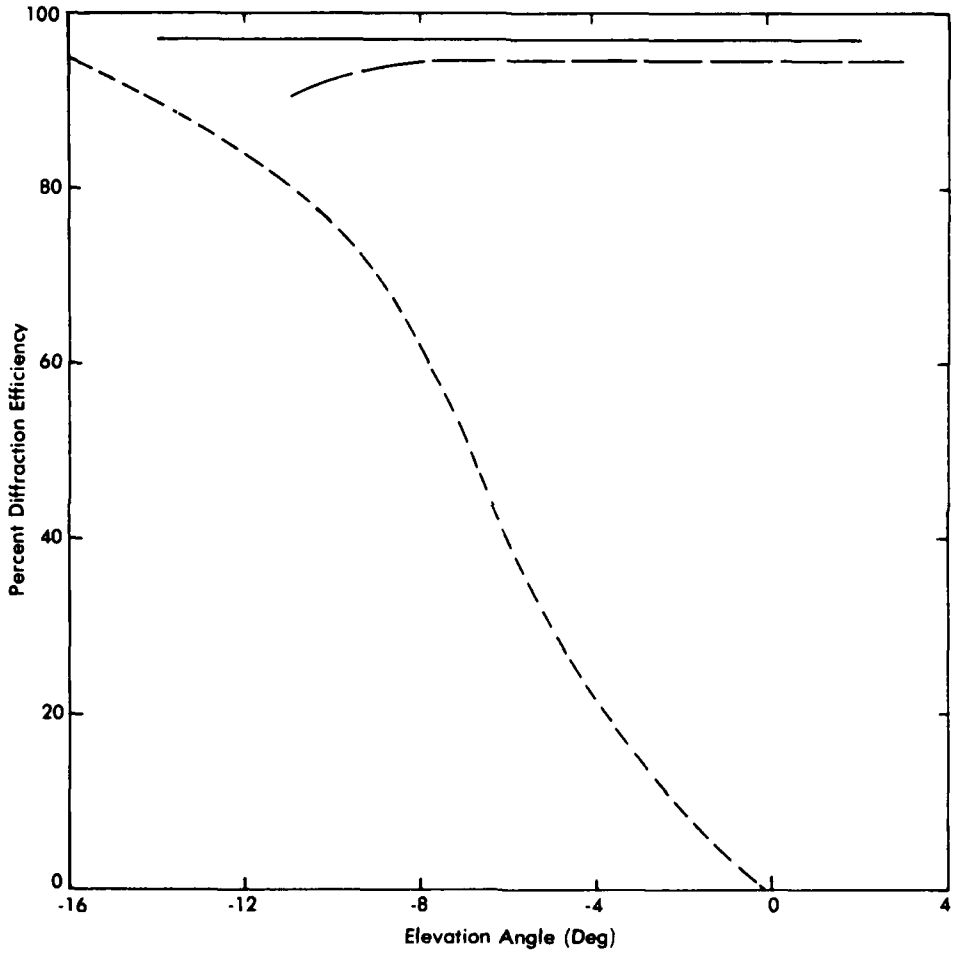


Figure 29. Hologram Efficiency As a Function of Vertical Field Angle for Rays Traced from Three Exit Pupil Locations. The solid line is for rays traced from the center of the pupil, the short dashes for rays from the top of the pupil, and the long dashes for rays from the bottom of the pupil.

bottom of the exit pupil would decrease at lower elevation angles. This compromise was not achieved as a result of using only a single ray from each end of the exit pupil to sample the hologram efficiency during the system optimization. It would have been helpful to have traced two rays from each end of the exit pupil. For a required vertical instantaneous field of 8° from the top and bottom of the exit pupil, for example, we would sample the hologram efficiency with rays at elevation angles of -8° and -16° from the top of the pupil, and at angles of +4° and -4° from the bottom of the pupil.

The region of low efficiency is limited to a relatively small portion of the exit pupil and field-of-view. Figure 30 shows efficiency curves for exit pupil locations 0.75 inch above and below the center of the pupil; these locations are half the distance to the limits of the pupil. The ray efficiencies plotted in Figure 30 exceed 88 percent, and over most of the field, are above 90 percent.

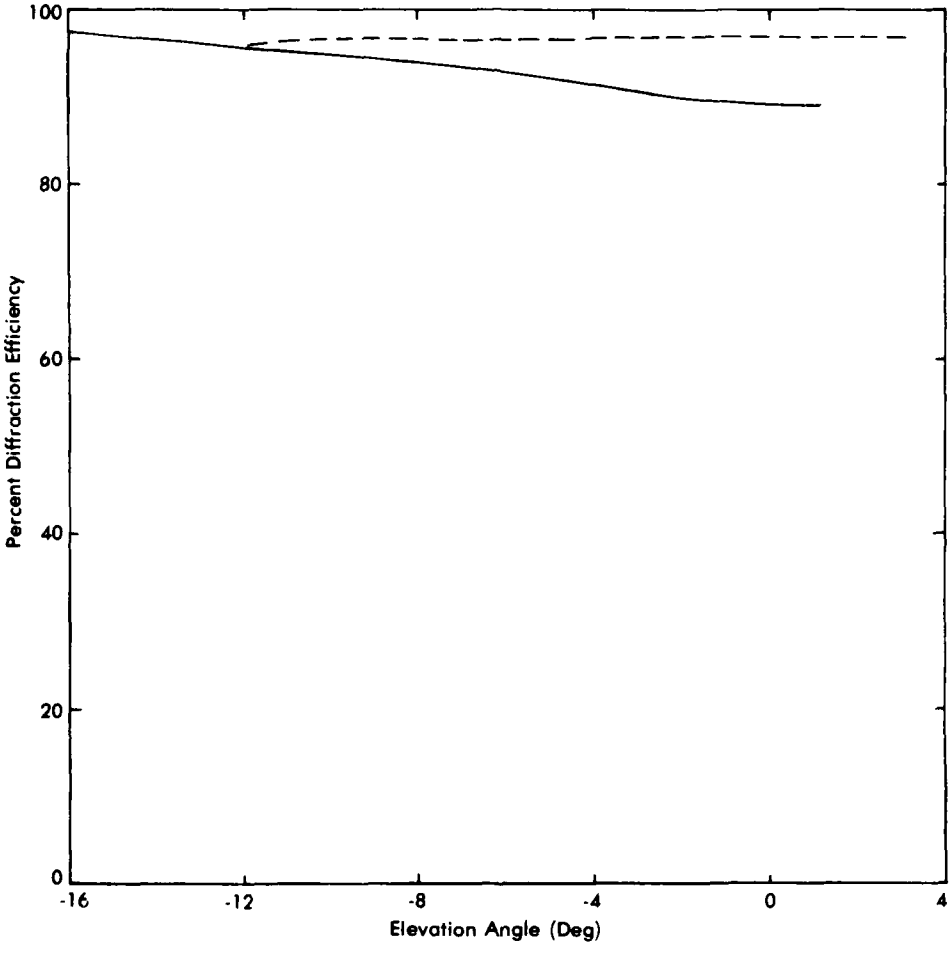


Figure 30. Hologram Efficiency As a Function of Vertical Field Angle for Rays Traced from Two Exit Pupil Locations. The solid line is for rays traced from 0.75 inch above the pupil center; the dashed line for rays traced from 0.75 inch below the pupil center.

AD-A113 982 ENVIRONMENTAL RESEARCH INST OF MICHIGAN ANN ARBOR RA--ETC F/G 14/5
DESIGN STUDY FOR A LOW-DISTORTION HOLOGRAPHIC HUD.(U)
JAN 82 W S COLBURN, R C FAIRCHILD F33615-80-C-1077
UNCLASSIFIED ERIM-150800-29-F AFWAL-TR-81-1263 NL

# SECTION VI
# REALIZATION OF CONSTRUCTION BEAMS

The discussion thus far has considered the construction beams to be defined simply by a description of their respective phase variations at the hologram. Aside from the analysis in Section II proving the realizabilty of the phase functions, we have not considered how the construction beams would be implemented to fabricate the aspheric combiner. In this section, we discuss practical considerations for the realization of the analytically defined construction beams.

## 1. DESIGN PROCEDURE

The form in which the construction wavefronts are described does not suggest a direct method for their generation. A conceptually straightforward method would be to record the combiner itself as a computer generated hologram (CGH) [9]. This method, however, is impractical because of limitations in present-day CGH fabrication technology. Recording devices that are used to fabricate CGHs are limited in resolution to spatial frequencies that are far below those required for the combiner. CGHs, moreover, are not formed as volume holograms, and they generally produce unwanted diffracted orders in addition to the desired diffracted order.

By combining a CGH with conventional optical elements, we can make use of its capability for forming arbitrary phase variations that might otherwise be unrealizable. For this method, the desired construction wavefront at the combiner is formed by an optical system in which conventional elements provide the basic shape and the CGH adds small but irregular phase perturbations to the wavefront. In addition, the conventional elements are arranged so that there is a plane where a spatial filter, or aperture, can be located to block unwanted orders diffracted by the CGH.

The task, then, of designing a construction beam is as follows. Starting with a spherical wavefront diverging from a point source, an optical system is required that will provide the desired phase variation at the hologram surface, and at an intermediate location form a real image of the point source where a spatial filter can be located. Figure 31 shows the form that such an optical system might have.

Since we are given the wavefront description at the hologram, we can analyze the construction beam in the reverse direction, tracing rays away from the hologram toward the point source. For a system having the form shown in Figure 31, the objective is to select conventional optical elements that focus the wavefront to the intermediate point focus at the spatial filter plane, and then to a second point focus that will be the location of the construction beam point source. The quality of the intermediate point focus need only be sufficient to permit separation of the orders diffracted by the CGH. The point focus at the point source location also does not need to be of high quality as the final correction will be provided by the CGH. The point focus must be good enough, however, so that the amount of correction required by the CGH is within its information capacity.

## 2. CGH BANDWIDTH

The major limitation of the CGH is the limited bandwidth of the information it can record. For a Burch type CGH [10] recorded at a resolution (or spot size) of $\delta x$, the maximum bandwidth $\Delta f$ of the information that can be recorded is

$$\Delta f = \frac{1}{2\delta x}$$

For the Optronics Model 1600 film recorder at ERIM, $\delta x$ = 50 μm and $\Delta f$ = 10 cycles/mm. For a recorder that has a 5 μm spot size, $\Delta f$ = 100 cycles/mm, which is a reasonable upper limit for current recorders.

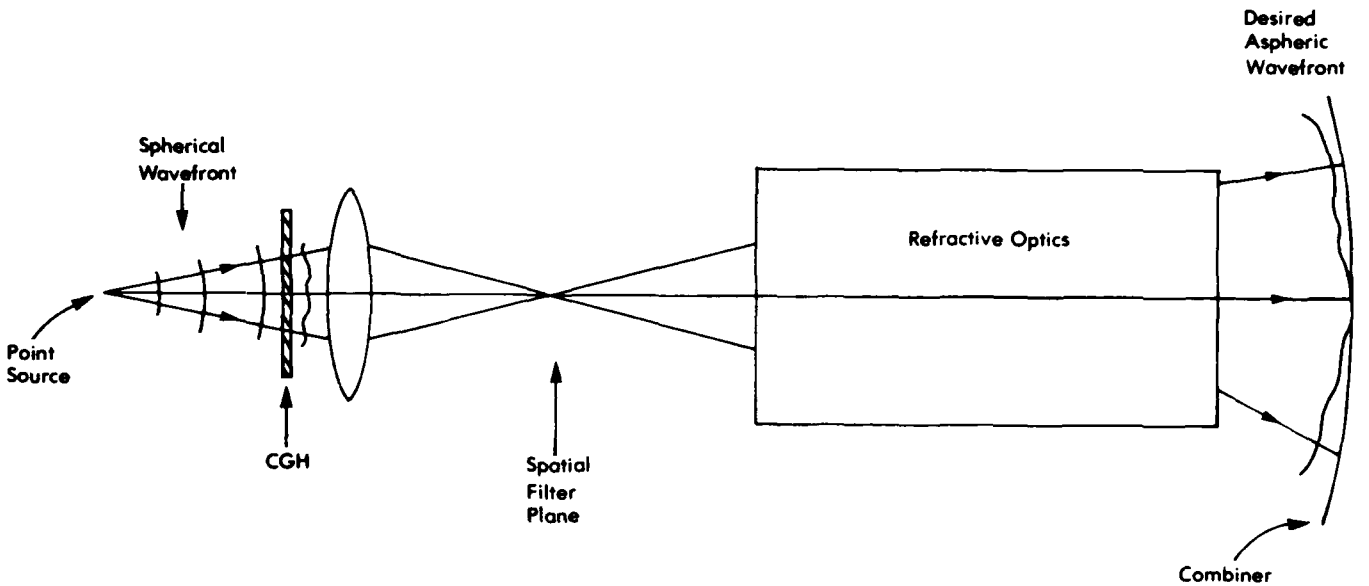


Figure 31. Construction Beam Optical System

Referring to Figure 31, the CGH converts a spherical wavefront into the wavefront required by the construction beam design. The required CGH bandwidth can be found from an analysis of the diffraction required by the hologram. We can express the grating equation in the form

$$\frac{1}{f_x}(l_d - l_i) = \lambda \tag{48a}$$

$$\frac{1}{f_y}(m_d - m_i) = \lambda \tag{48b}$$

where $f_x$ and $f_y$ are the grating spatial frequencies in the x and y directions, respectively, l and m are ray direction cosines, and the subscripts i and d represent the incident and diffracted rays, respectively. Solving for $f_x$ and $f_y$, we have

$$f_x = \frac{l_d - l_i}{\lambda} \tag{49a}$$

$$f_y = \frac{m_d - m_i}{\lambda} \tag{49b}$$

By tracing rays from the hologram to the CGH plane, we can find the direction cosines of the rays after diffraction, and knowing the location of the point source gives the direction cosines of the incident rays. If we assume that the CGH lies in the xy-plane, and that the point source is on the z-axis a distance $z_o$ from the CGH, the direction cosines of the incident rays at a point (x,y) on the CGH are

$$l_i = \frac{x}{R}$$

$$m_i = \frac{y}{R}$$

where $R = (x^2 + y^2 + z_o^2)^{1/2}$. Equations (49) can then be written as

$$f_x(x,y) = \frac{1}{\lambda}\left[ l_d(x,y) - \frac{x}{R} \right] \tag{50a}$$

$$f_y(x,y) = \frac{1}{\lambda}\left[ m_d(x,y) - \frac{y}{R} \right] \tag{50b}$$

The required bandwidths $\Delta f_x$ and $\Delta f_y$ of the CGH can be determined by searching over the CGH to find the maximum and minimum spatial frequencies required, with

$$\Delta f_x = (f_x)_{max} - (f_x)_{min}$$

$$\Delta f_y = (f_y)_{max} - (f_y)_{min}$$

In a previous investigation reported in Reference 1, we used a CGH that had maximum bandwidths in both x and y directions of less than 1 cycle/mm. Analysis of a construction beam similar to the final combiner reference beam indicated that without the auxiliary conventional optics, the required CGH bandwidths would be $\Delta f_x$ = 70 cycles/mm and $\Delta f_y$ = 270 cycles/mm. The addition of conventional optics to provide basic wavefront shaping reduced the required CGH bandwidths to 30 and 20 cycles/mm, respectively; these fall within the capabilities of existing recording devices.

## SECTION VII
## CONCLUSIONS AND RECOMMENDATIONS

The design investigation of a low-distortion HUD optical system demonstrated the usefulness of aspheric holograms that have analytically defined construction wavefronts. These holograms not only offer a great deal of design flexibility, but also permit the designer to concentrate on the hologram itself, postponing the design of the construction beams until the hologram design is complete. Previous design methods have required complete specification of both construction beams, including all required optical components, prior to the hologram ray trace. A key to the application of analytically defined construction wavefronts is the use of computer generated holograms, which greatly increases the flexibility of the construction wavefront design, permitting the specification of wavefronts that would be difficult or impossible to realize with conventional optics alone.

From our design investigation of a low-distortion HUD optical system, we conclude that distortion correction to the goal of 0.5 percent is feasible using the approach of the aspheric holographic combiner. Although our design did not meet the goal over the entire field-of-view, we believe that with additional effort, we would have continued to obtain improved performance. More work was also required on the design to reduce the errors, especially the parallax errors. Some modifications to the merit function structure would be useful to provide for direct parallax computations, so that the parallax errors would receive greater attention during the optimization process. In order to concentrate on evaluating the capability of our approach to correct distortion, we limited the design optimization to the instantaneous field-of-view (12°V x 20°H). Further optimization of the design should be expanded to cover the total field-of-view (20°V x 20°H). We found, on the other hand, that once the

initial aspheric combiner design had been established, further optimization of the combiner design alone was not fruitful. The most meaningful results were obtained from optimization of the system as a whole, based on complete system performance.

For the design we have reported on in this report, further work is recommended along the lines described above. We also recommend continued investigation of aspheric holograms at a more basic level. The investigation of holographic imagery from the point-of-view of minimizing the wavefront error as described in Section II warrants continued study. The investigation of other methods, such as Zernike polynomials, for describing the construction wavefronts may result in significant improvements in hologram flexibility and performance. Of interest specific to the HUD application would be an investigation of coma correction in the combiner by means of improved construction wavefront design, as coma is the dominant aberration after correction of astigmatism, and furthermore, coma correction in the relay lens accounts for much of the decentering and tilting of the relay lens elements. It would also be of interest to investigate the introduction of one or more additional aspheric holographic elements into the optical system with the objective of simplifying the conventional optics portion of the relay lens.

## SECTION VIII
## REFERENCES


1. Fairchild, R.C. and J.R. Fienup, "Computer-Originated Hologram Lenses," Proceedings of the SPIE, Recent Advances in Holography, Volume 215, February 1980.

2. Au, A., A. Graube, and L.G. Cook, "Holographic Lens for Pilot's Head Up Display - Phase IV," Technical Report No. NADC 78-191-60, Hughes Research Laboratories.

3. Fienup, J.R., ERIM Internal Memo No. EO-80-2097, April 1980.

4. Spencer, G.H. and M.V.R.K. Murty, "General Ray-Tracing Procedure," J. Opt. Soc. Am., 52, 672, 1962.

5. Welford, W.T., "A Vector Raytracing Equation for Hologram Lenses of Arbitrary Shape," Opt. Comm., 14, 322, 1975.

6. Kogelnik, H., "Coupled Wave Theory for Thick Hologram Gratings," Bell Sys. Tech. Journal, 48, 2909, 1969.

7. Kaplan, W., "Advanced Calculus," First Edition, Addison-Wesley, pp. 244-249, 1959.

8. Latta, J.N. and R.C. Fairchild, "New Developments in the Design of Holographic Optics," Proc. of the SPIE 39, Applications of Geometrical Optics, 107 (1973); J.N. Latta, "Computer-Based Analysis of Holography Using Ray Tracing," Appl. Opt. 10, 2698 (1971).

9. Lee, W.H., "Computer-Generated Holograms: Techniques and Applications," in E. Wolf, ed., Progress in Optics, Vol. 16 (North-Holland, 1978).

10. Burch, J.J., "A Computer Algorithm for the Synthesis of Spatial Frequency Filters," Proc. IEEE 55, 559, 1967.




*U.S.Government Printing Office: 1982 — 559-004/3027